Journal of Membrane Science 689 (2024) 122134

Contents lists available at ScienceDirect

Journal of Membrane Science

journal homepage: www.elsevier.com/locate/memsci

# Dissolved gas recovery from water using a sidestream hollow-fiber membrane module: First principles model synthesis and steady-state validation

I. Song [a], P.S. Soulia [a], P.J. Novak [b], W.A. Arnold [b], N.C. Wright [a,*]

[a] Mechanical Engineering Department, University of Minnesota, Twin Cities, United States of America
[b] Civil, Environmental, and Geo-Engineering Department, University of Minnesota, Twin Cities, United States of America

ARTICLE INFO

*Keywords:*
Hollow-fiber membrane
Gas recovery
Anaerobic digestion

ABSTRACT

This paper presents a first-principles model for the recovery of dissolved gases from liquids using a sidestream hollow-fiber membrane module. The model avoids the use of new empirical coefficients, thus providing a parametric understanding of the process behavior for future design and optimization of membrane modules. This type of first-principles model could be particularly useful when gas recovery is beneficial to biological or chemical reactions of interest, such as the acetogenesis reactions in two-stage anaerobic digesters. The steady-state behavior of the model was validated against both new experimental data for the recovery of $H_2$, $CH_4$ and $H_2$–$CH_4$ mixtures from pure water, as well as existing published data. The modeled gas recovery predictions agreed with experimental data to an absolute average error of 13%, and an average $R^2$ value of 0.98. Parametric analysis of mixed-gas recovery suggests possible key transition points in the composition of the recovered gases. For example, at 40 °C, increasing trans-membrane pressure while keeping hydraulic residence time (HRT) under 0.5 s will result in an increase in the ratio of $H_2$ to $CH_4$ recovered. Otherwise, increasing trans-membrane pressure will instead decrease the ratio of $H_2$ to $CH_4$ recovered. The model has potential to be extended to transient analysis, but has yet to be validated with transient experimental data. This model was successfully implemented in both Python and MATLAB, and provides valuable insights for future net-energy optimization for anaerobic digestion systems with in-situ gas recovery.

## 1. Introduction

Wastewater treatment accounts for approximately 1% of global energy consumption [1], 30%–50% of municipal energy consumption, and 3% of global greenhouse gas (GHG) emissions [2] around the world. In 2015, the United Nations General Assembly ratified a set of Sustainable Development Goals (SDGs), some of which refer to increasing access to sanitation and halving the proportion of untreated wastewater discharge (SDG 6.2-6.3) [3]. The International Energy Agency (IEA) estimates that the achievement of SDG 6.2 and 6.3 with current wastewater treatment technologies would result in a 6-fold increase in energy consumption by wastewater treatment plants (WWTPs) [2]. There is a pressing need, therefore, to develop technologies that can increase the efficiency of, and recover energy from, wastewater treatment processes. While the recovery of methane ($CH_4$) from the effluent of various single-stage anaerobic digestion (AD) processes via the use of hollow-fiber (HF) membrane contactors has been studied [4–7], this work focuses on the combination of gas recovery in the form of $H_2$ and $CH_4$ for application to small-scale two-stage AD processes.

In the United States, wastewater is generally treated in a centralized WWTP. The treatment process converts organic substrates contained in the wastewater to $CO_2$ and waste biosolids. The strength of the organic wastewater is commonly described by its chemical oxygen demand (COD). Before entering the plant, different wastewater streams — low-strength wastewater from household use (~150–300 mg/L COD) and high-strength wastewater from industrial manufacturing facilities (~5000–35,000 mg/L COD) - are mixed together, diluting the net strength of the wastewater and making it more difficult to recover energy from these high-strength streams. Industries that release high-strength wastewater are also often required to pay strength charges to the city to account for the additional energy requirement.

* Corresponding author.
*E-mail address:* natasha@umn.edu (N.C. Wright).

https://doi.org/10.1016/j.memsci.2023.122134
Received 2 July 2023; Received in revised form 13 September 2023; Accepted 2 October 2023
Available online 6 October 2023

**Nomenclature**

| | |
|---|---|
| $C_j$ | Concentration of species $j$ (mol m$^{-3}$) |
| $D$ | Inner diameter of the hollow-fiber (m) |
| $D_{j,H_2O}$ | Diffusion coefficient of gas $j$ in water (m$^2$ s$^{-1}$) |
| $J_j$ | Flux of species $j$ through the membrane (mol m$^{-2}$s$^{-1}$) |
| $k_g$ | Gas mass transfer coefficient (m s$^{-1}$) |
| $k_l$ | Liquid mass transfer coefficient (m s$^{-1}$) |
| $K_{tot}$ | Total mass transfer coefficient (m s$^{-1}$) |
| $L$ | Membrane Length (m) |
| $MW_j$ | Molecular weight of species $j$ (g/mol) |
| $n$ | Number of segments |
| $P_0$ | Permeate-side pressure (Pa) |
| $Perm_j$ | Permeability of gas $j$ (Barrer) |
| $Q$ | Volumetric flowrate (m$^3$ s$^{-1}$) |
| $R$ | Universal Gas Constant (J K$^{-1}$ mol$^{-1}$) |
| $T$ | Temperature (K) |
| $V$ | CSTR volume (m$^3$) |
| $\bar{V}_j$ | Molar volume of component $j$ (mol m$^{-3}$) |
| $V_L$ | Volume of the lumen (m$^3$) |
| $V_S$ | Volume of the shell (m$^3$) |
| $y_j$ | Mole fraction of gas $j$ in the permeate |

**Dimensionless numbers**

| | |
|---|---|
| Gr | Graetz Number |
| Re | Reynolds Number |
| Sc | Schmidt Number |

**Greek symbols**

| | |
|---|---|
| $\delta$ | Membrane wall thickness (m) |
| $\phi$ | Wilke-Chang association constant |
| $\mu$ | Viscosity (Pa s) |

**Subscripts**

| | |
|---|---|
| $i$ | Lumen segment index |
| $j$ | Species component index |

The high energy cost of centralized wastewater treatment has led to an increased interest in the decentralized (on-site) treatment of high-strength organic wastewater and the potential for energy recovery from such processes [8,9]. Two-stage AD processes have been proposed as an alternative to single-stage AD processes [10,11]. In a two-stage AD process, hydrolysis and fermentation occur in the first stage reactor, producing $H_2$ and $CO_2$. Methanogenesis – the final step in the AD process – and some acetogenesis occur in the second-stage reactor, producing $CH_4$ and $CO_2$. Separating the AD process into two steps allows for separate optimization of operating parameters, particularly the temperature and pH, for the fermentation and methanogensis processes. Additionally, gas recovery can be performed on both reactor stages, thereby allowing for energy recovery in the form of biogas, more specifically known as biohythane [12,13]. The removal of $H_2$ from the first-stage reactor is also expected to accelerate the disintegration of long chain fatty acids and volatile fatty acids into acetic acid due to the inhibitory nature of $H_2$ to the acetogenesis process [14].

The recovery of energy from AD processes has been an active area of research [9,15–18]. This recovered energy comes from the gases produced and the solids left at the end of the AD process. The produced gases, known as biogas, are mostly composed of $CH_4$ and $CO_2$. Most biogas recovery methods collect the gases from the headspace of the reactor [19,20]. A significant portion of the $CH_4$ produced in the AD process, however, remains dissolved in the liquid [20]. Crone et al. report that 19%–63% of total $CH_4$ produced in anaerobic membrane bioreactors (AnMBRs) is lost via the effluent [20], representing a significant loss in the energy recovered, and a significant contributor to the greenhouse gas emissions of the wastewater treatment process [8]. This has led to research aimed at polishing methods to recover $CH_4$ from the effluent stream. These methods include air-stripping [9] and $CH_4$ recovery through membrane contactors (Table 1).

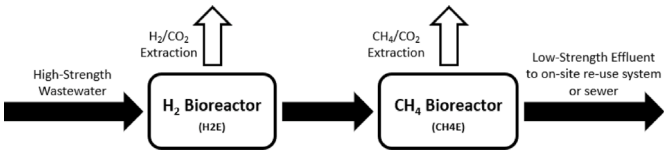


**Fig. 1.** Diagram of the two-stage AD system proposed by Chen et al. (2022) [25]. Each bioreactor is seeded with encapsulated bacterial colonies that can be optimized for the specific bioreactor. Active gas recovery will be performed on both bioreactors. The first bioreactor is predicted to recover primarily $H_2$ and $CO_2$, while the second bioreactor is predicted to recover primarily $CH_4$ and $CO_2$. The recovered gas flows can be combined to produce biohythane for energy recovery.

The use of hollow fiber membrane contactors (HFMC) for gas recovery is a promising method of recovering gases from AD effluent and is the focus of this work. HFMCs have two different operating modes. Lumen side HFMC operation, where the liquid phase flows inside the lumen, tends to allow for higher mass transfer coefficients in the liquid phase, but is susceptible to clogging as a result of the high solids content in the liquid. Shell side operation is less susceptible to clogging, but generally has poorer mass transfer coefficients at higher flowrates due to hydrodynamic channeling.

The driving force for mass transfer through HFMCs is generated by using either a sweep gas or a vacuum. The choice between the two depends on both the terminal use of the recovered gases and the membrane material. Sweep gas operation is commonly used when the HFMC is porous, because it reduces the risk of pore-wetting and allows for high gas-side mass transfer coefficients. Unfortunately, the recovered gas is significantly diluted by the sweep gas. Vacuum operation is more common with non-porous membranes and results in high purity gases, but requires more energy to maintain the TMP.

Chen et al. recently proposed an encapsulated two-stage AD process – known as the modular encapsulated two-stage anaerobic biological (METAB) system – where the bacteria responsible for the acetogenesis and methanogenesis are retained in polymeric beads, allowing for the separation of hydraulic and solids residence time (Fig. 1) [25]. Given the recent successes of removing dissolved $CH_4$ and $CO_2$ from anaerobic effluent, the removal of $H_2$ and $CO_2$ gases from the METAB first-stage reactor is also plausible. Removal of $H_2$ could allow for energy recovery and increase AD reaction rates. Additionally, the use of encapsulated bacteria is also potentially beneficial for lumen-side HFMC operation, as it could reduce fouling of the HFMC.

To accurately model biohythane production and its effects on the rate of acetogenesis in the first-stage reactor, a gas extraction/recovery model is critical. In this work, our goal was to create a first-principles model for the removal of gases from the METAB system, avoiding new empirical parameters that fit the model directly with experimental gas recovery data. This allows the development of a parametric understanding of the process behavior, thus enabling future design and optimization of novel membrane architectures.

The removal or addition of gases from fluids using a side-stream HFMC has been a topic of interest in many application areas, including dissolved oxygen removal [26], blood oxygenators [27,28], biogas removal from wastewater effluent [4], and process intensification technologies [29]. Previous literature presents the various effects of operating parameters on HF membrane operations, both from an

**Table 1**
Summary of previous experimental work on $CH_4$ and $CO_2$ removal using HFMCs and various feed types, including expanded granular sludge bed (EGSB), upflow anaerobic sludge blanket (UASB), AnMBR and synthetic wastewaters.

| Membrane material | Membrane characteristics | Feed type | Liquid flow | Driving force | Maximum removal efficiency [%] | Ref |
|---|---|---|---|---|---|---|
| PDMS | Dense | EGSB | Shell | Sweep | 72% $CH_4$ | [21] |
| PDMS | Dense | Synth, UASB, AnMBR | Shell | Sweep | 92.6% $CH_4$ | [4] |
| PP | Microporous | Synth, UASB, AnMBR | Lumen | Sweep | 98.9% $CH_4$ | [4] |
| PDMS | Dense | AnMBR | Shell | Vacuum | ~80% $CH_4$ | [22] |
| PP | Microporous | Synth | Lumen | Sweep | 97% $CH_4$ | [23] |
| PP/PU | Composite | UASB | Shell | Vacuum | 97% $CH_4$ | [5] |
| PDMS | Dense | EGSB | Both | Vacuum and Sweep | 77% $CH_4$ | [7] |
| PP | Microporous | Synth, AnMBR | Lumen | Sweep | 95.7% $CH_4$, 76.2% $CO_2$ | [24] |

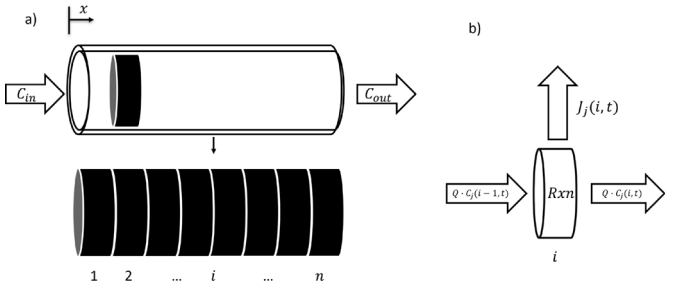


**Fig. 2.** This figure depicts how the hollow-fiber lumen-side model is formulated. (a) A single hollow fiber tube is assumed to act as an ideal plug flow reactor (PFR), and split into $n$ segments. (b) A mass balance can be drawn around each segment for each gas species $j$, which includes species entering and leaving due to the advection, species leaving due to permeation $J$ (molar flux), and a reaction term $Rxn$ (if applicable).

experimental and modeling perspective. Many of the models have either focused on averaged concentrations to lump the membrane model into a black box [22], or calculate their own overall mass transfer correlations for various membrane modules [26]. Those that focus primarily on using first principles, use a steady-state assumption [6,30].

This work presents modeling of HF gas recovery that could be extended to transient analysis. Model-predicted performance was compared to experimental performance via bench-scale experiments recovering $H_2$, $CH_4$, and $H_2$-$CH_4$ from water. The presented model could, in the future, be combined with a biochemical process model to capture the change of reaction rates in the first-stage reactor, and therefore allow for dynamic modeling of the entire METAB system.

## 2. Model derivation

### 2.1. Model structure and assumptions

A single hollow fiber membrane was discretized into $n$ control volumes (segments) of length $L/n$ (Fig. 2). We treated the hollow fiber as an ideal plug-flow reactor (PFR), with flow entering and exiting at a constant volumetric flowrate $Q$. There also exists a continuously stirred tank reactor (CSTR) from which the flow originates from and returns. We performed a mass balance on each control volume to determine the rate at which gases were recovered out of a single fiber, $J$. Therefore, the model tracked the concentration of each gas species $j$ in each segment $i$ of the lumen, the concentration of each gas species in the CSTR, and the concentration of each gas species in the shell of the module.

The assumptions for the membrane module model are listed below:

1. The liquid in the reactor was well-mixed, and acted as an ideal continuously stirred tank reactor (CSTR).
2. The flow of the liquid in the lumen of the hollow-fiber membranes could be approximated as a PFR, but the concentration gradient of the gases were modeled as a boundary-layer resistance.
3. The shell side of the hollow-fiber membrane module (the permeate) had uniform pressure at the vacuum pressure. The gas along each shell-side segment of the hollow-fiber module was well-mixed, but there were varying partial pressures between segments.
4. The gas boundary layer resistance on the permeate/shell side of the membrane was negligible compared to the resistances from the liquid boundary layer and the membrane.
5. The gases present ($N_2$, $O_2$, $CH_4$, and $H_2$) did not significantly interact with each other both in the liquid or the gas phases. The only interaction between them was that the simultaneous permeation of multiple gases resulted in higher driving forces.
6. The mass transport in the flow direction was dominated by convection, while the mass transport in the direction perpendicular to the flow was affected by both diffusion and convection.
7. The effects of temperature gradients from viscous dissipation and from temperature differences between the fluid media and the air surrounding the membrane module were neglected.
8. All of the gases were treated as ideal gases.
9. Hollow fiber spacing was consistent, and each hollow fiber in the module performed identically.
10. Diffusion through the dense PDMS membrane happens only through the solution–diffusion mechanism.

### 2.2. Mass conservation

Mass conservation equations for each segment tracked the change in concentration of each species in the segment. The segments are enumerated from 1:n (Fig. 2). Because we also had to track the concentration in the CSTR reactor, we included the concentration of "Segment 0", or $i = 0$, which indicated the concentration of each species of gas in the CSTR reactor. The set of mass balance equations are shown below in Eqs. (1a) and (1b).

$$\frac{dC_j(i,t)}{dt} = \frac{Q}{dV}(C_j(i-1,t) - C_j(i,t)) - \frac{K_{tot,j}(i)}{D/4}\left(C_j(i,t) - \frac{y_j(i,t)P_0}{H_j}\right), i = 1:n \quad (1a)$$

$$\frac{dC_j(0,t)}{dt} = \frac{Q}{V_{\text{tank}}}(C_j(n,t) - C_j(0,t)) \quad (1b)$$

In the equations above, $C_j(i,t)$ is the concentration of species $j$ in segment $i$ and time $t$. $Q$ is the volumetric flowrate, $dV$ is the volume of a segment. $K_{tot,j}(i)$ is the total mass transfer coefficient of species $j$ in segment $i$, while $D$ is the inner diameter of the fiber. $y_j(i,t)$ is the partial pressure of species $j$ in the shell-side of segment $i$ at time $t$. $P_0$ is the vacuum pressure, and $H_j$ is the Henry's Law constant for species $j$. Finally, $V_{\text{tank}}$ is the volume of the CSTR reactor.

Note that the term $\frac{K_{tot,j}(i)}{D/4}$ comes from the governing equation for flux through a membrane. Because the left hand side of the equation is the change in concentration with respect to time, a conversion factor of $\frac{dA}{dV}$ is needed.

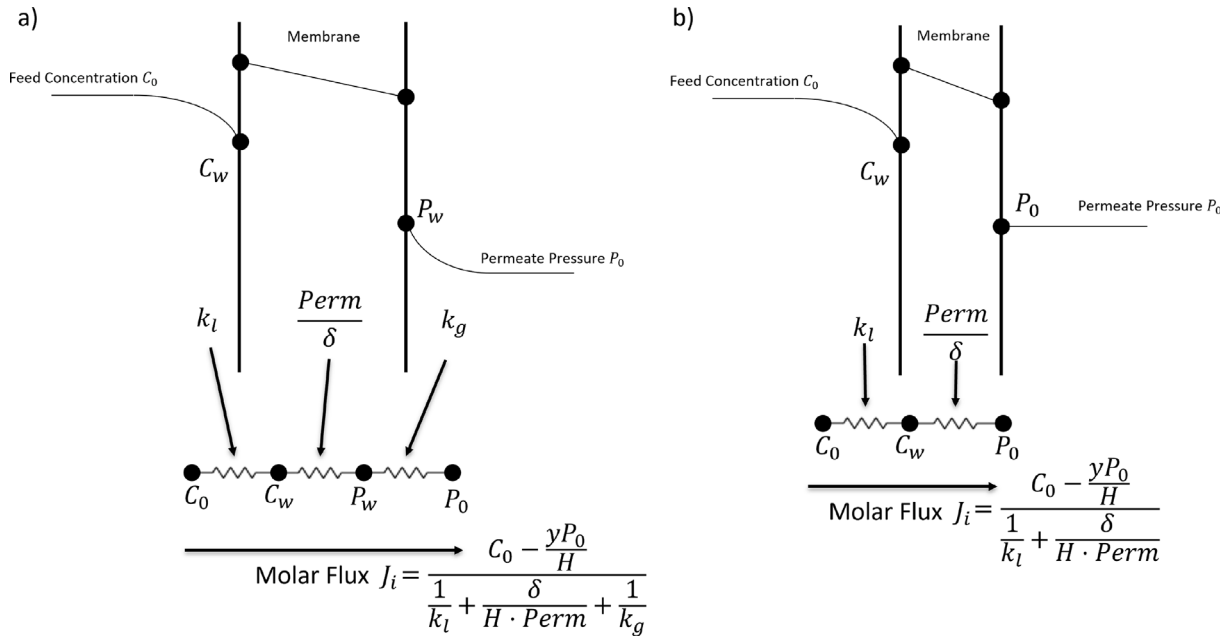


**Fig. 3.** Resistance network diagram for the transport of a gaseous species from the bulk liquid to the vacuum permeate at pressure $P_0$. Three resistances are shown in (a). In order from left to right, they are: the liquid boundary-layer, the membrane, and the gas boundary layer. The gas boundary layer is omitted in (b) due to the commonly proven assumption that $k_g \gg k_l$.

### 2.3. Mass transport

The mass transport of the gases from the bulk solution to the vacuum permeate was modeled as a resistance network (Fig. 3). It is common practice, however, to neglect the boundary layer resistance on the gas side because diffusion coefficients in gases are a few orders of magnitude higher than diffusion coefficients in liquids ($k_g \gg k_l$). This assumption has also been demonstrated in the case of membrane pervaporation by Crowder & Cussler [31]. Here, we retain the membrane mass transfer coefficient, and the equation that relates the molar gas flow rate from the bulk of the flow to the permeate is,

$$J_j(i,t) = K_{tot,j}(i)\left(C_{0,j} - \frac{y_j(i,t-1)P_0}{H_j}\right) = \frac{\left(C_{0,j} - \frac{y_j(i,t-1)P_0}{H_j}\right)}{\frac{1}{k_{l,j}} + \frac{\delta}{H_j \cdot Perm_j}} \quad (2)$$

where $J_j(i,t)$ is the molar flux of species $j$ from segment $i$ at time $t$. For a gas species $j$, $y_j$ is the partial pressure on the permeate side, $H_j$ is the Henry's Law coefficient, $Perm_j$ is the permeability of the membrane, $k_{l,j}$ is the liquid-side mass transfer coefficient that can be calculated by Eq. (6), and $C_{0,j}$ is the bulk gas concentration in the feed-side. $\delta$ is the thickness of the membrane, and $P_0$ is the operating pressure on the permeate side.

Membrane permeability values for each gas were provided by the manufacturer of the PDMS membrane modules [32]. These values were used in the model to calculate the mass transfer resistances that corresponded to transport through the membrane. This left two other unknowns in Eq. (2), which are the liquid-side mass transfer coefficient $k_{l,j}$ and the permeate partial pressure $y_j(i)$.

To model the liquid-side mass-transfer resistance, we first determined the ranges of Schmidt (Sc) and Reynolds (Re) numbers relevant to the experiments. The manufacturer data sheet for the hollow-fiber membrane module PDMSXA1000 (Permselect©, MedArray Inc., USA) used in this study suggested that common volumetric flowrates should range from 0.05 to 0.8 $m^3$/s, which corresponds to linear flow velocities between 2.3 cm/s and 36.7 cm/s. Therefore, the expected range of the Schmidt ($4 < Sc < 688$) and Reynolds ($4 < Re < 69$) numbers at 20 °C leads to the assumption that $Sc \gg Re$, implying that the velocity boundary layer will develop much faster compared to the mass-transfer boundary layer. Therefore, we initially assumed a fully-developed velocity profile and a developing mass-transfer boundary layer.

These assumptions are similar to those made in an analogous heat transfer problem known as the Graetz problem. For a developing mass-transfer boundary layer, it has been consistently shown that the Leveque solution is able to successfully predict the liquid mass transfer coefficient when it is flowing in the lumen of a hollow fiber module [33–35]. The Leveque solution is as follows:

$$Sh = 1.6151 Gz^{1/3} \quad (3)$$

where the Sherwood number is defined as $Sh = \frac{k_l}{D_j/D}$. $D_j$ is the diffusivity of the species in question, and $D$ is the characteristic length scale, taken here to be the inner diameter of the hollow-fiber. The Graetz number is defined as $Gz = ReSc\frac{D}{L}$, where $L$ is the length of the hollow-fiber membrane.

The Leveque solution was derived under the assumption that the thickness of the heat or mass transfer boundary layer is much smaller than the radius of the tube. As we approach regions where that assumption is no longer valid (i.e. slow flows or long tubes), then the Leveque approximation begins to fail, as the diffusion layer reaches the center of the tube. Newman derived an extension to the Leveque approximation [36]. The Newman extension is:

$$Sh(i) = 1.6151 Gz^{(1/3)} - 1.2 + 0.28057 Gz^{(-1/3)} \quad (4)$$

One important note about Eqs. (3) and (4) is the use of an averaged Graetz number. Initial derivations tended to use the local Graetz number, to account for the growth of the mass-transfer (or heat-transfer) boundary layer [37]. Recent papers, however, have mostly used the average Graetz number with Eq. (3). We approximated the mass-transfer entry length using a modified expression reported by Bergman et al. (Eq. (5)), which showed that the mass transfer boundary layer is developing (within the mass-transfer entry length) in 10%–76% of the hollow fiber [38]. Using an averaged Graetz number should not account for the enhanced mass transfer coefficients during the development of the boundary layer. Eqs. (3) and (4) and the use of the local and averaged Graetz numbers has been tested against published

deoxygenation data for the membrane used in the experiments (see below). Based on the results described in Section 4.1, Eq. (3) was used to determine the appropriate Sherwood number.

$$\left(\frac{x_{fd,m}}{D}\right)_{\text{lam}} \approx 0.05\text{Re}_D\text{Sc} \tag{5}$$

Finally, we can calculate the liquid-side mass transfer coefficient for each gas at each segment through the definition of the Sherwood number:

$$k_{l,j}(i) = \frac{Sh(i) \cdot D_{j,\text{H}_2\text{O}}}{D} \tag{6}$$

where $D_{j,\text{H}_2\text{O}}$ is the diffusion coefficient of species $j$ in $\text{H}_2\text{O}$.

The last part of the mass transfer model is the calculation of the permeate side mole fraction $y_j(i)$. To do this, we used a finite difference method, where we assumed an initial pressure distribution among the gases in the permeate. We then used Eq. (1a) to calculate the change of concentration in the lumen. The new concentration in the shell after the permeation occurs is:

$$C_{j,shell}(i,t) = \frac{y_j(i,t-1) * P_0}{RT} + \frac{dC_j(i,t)}{dt}\frac{V_L}{V_S} \tag{7}$$

where $V_L$ and $V_S$ are the volumes of the membrane contactor lumen and shell, respectively. We can then use these new concentrations to calculate the new permeate partial pressures at time $t$:

$$y_j(i,t) = \frac{C_{j,shell}(i,t)}{\sum_j C_{j,shell}(i,t)}dt \tag{8}$$

This method of approximating $y_j(i,t)$ assumes that in each segment of the shell, the gases are well-mixed. Between each time-step, the gas equilibriates, and some of it leaves the shell due to the vacuum pressure that is exerted. This approximates each segment's shell-side as an ideal CSTR. This method also avoids having to solve for the concentration of the shell and lumen simultaneously which has also been done by Tan et al. in a different hollow fiber membrane configuration [26].

#### 2.3.1. Temperature dependence of gas properties

Many of the thermophysical properties of the substances that we are modeling vary significantly with temperature. Specifically, the kinematic viscosity of water, permeate partial pressure of water vapor, Henry's Law coefficients, and diffusion coefficients of the gases in water. To account for these temperature dependencies, we relied on correlations that have been previously reported.

An equation for the absolute viscosity of water was rigorously fitted by Huber et al. [39]. The liquid density of water as a function of temperature can be found from the American Institute of Chemical Engineers (AIChE) Design Institute for Physical Properties (DIPPR) Database, Equation # 100. The formula for the Henry's Law Coefficients was taken from the NIST Webbook.

Finally, the diffusion coefficients of the gases in water were initially calculated using the Wilke-Chang correlation [40]. The correlation is shown below:

$$D_{j,\text{H}_2\text{O}} = \frac{(7.4\times10^{-8})(\phi\text{MW}_{\text{H}_2\text{O}})^{0.5}T}{\mu\bar{V}_j} \tag{9}$$

where $\phi$ is the association constant, $\text{MW}_{\text{H}_2\text{O}}$ is the molar mass of water, $\mu$ is the viscosity of water, and $\bar{V}_j$ is the molar volume of component $j$. $\bar{V}_j$ is calculated from a correlation by Tyn and Calus (1975) as referenced in Poling et al. [41] and shown below:

$$\bar{V}_j = 0.285V_C^{1.048} \tag{10}$$

where $V_C$ is the critical molar volume of the gas, tabulated on the NIST Webbook.

The diffusion coefficients calculated from Eq. (9) were found to be significantly different from experimental values for $O_2$, $N_2$, $CH_4$ and $H_2$ that were reported by other authors [42–46]. To account for the difference, we adjusted the association parameter $\phi$ in Eq. (9) to the data presented by the papers above (Appendix B). This resulted in an association parameter of 9.84 for $H_2$, 2.2 for $CH_4$, 1.77 for $N_2$ and 1.90 for $O_2$ in comparison with Wilke and Chang's reported association parameter of 2.6 for any gas in water [40]. Through this fitting, we maintained the dependence of the diffusion coefficient on both temperature and water viscosity. It was important that the diffusion coefficients were modeled accurately, because the model is particularly sensitive to gas diffusivity.

#### 2.3.2. Water vapor permeation

As described by Tan et al. water vapor permeation can increase the driving force for other gas permeation through a vacuum-driven membrane module [26]. In general, multi-component effects between non-reacting species will increase the mass transfer rate. If we assumed that there was no air permeating through the membrane at steady-state, we are likely to slightly underestimate the recovery of our gas of interest.

Tan et al. noted that water vapor permeation only increases the driving force slightly at room temperature [26]. However, as we increase temperature, the effect of water vapor permeation will significantly increase. To account for this, $H_2O$ was added as another permeating species, where the driving force on the lumen-side was simply the saturated water vapor pressure at the operating temperature, as described by Huang [47].

In this model, a total pressure boundary condition is enforced on the vacuum-side of the HFMC. If water vapor permeation is not accounted for, then this total pressure boundary condition $P_0$ is only composed of the dissolved gas species. For example, in the case of oxygen recovery from water, the vacuum-side of the HFMC will only be occupied by oxygen and nitrogen. However, accounting for the permeation of water vapor will reduce the permeate partial pressures of oxygen and nitrogen in the vacuum side, because we have introduced a third component, while holding the total pressure boundary condition $P_0$ constant.

## 3. Materials and methods

The model-predicted gas recovery rate was evaluated using a commercially available hollow-fiber membrane module (1000 $\text{cm}^2$ total membrane area). The objective was to assess the accuracy of the model over a diverse range of operating parameters (linear flow velocity, shell-side vacuum pressure, temperature, and gas composition) without conducting prior system characterization.

### 3.1. Experimental apparatus

The experimental setup (Fig. 4) utilized a commercially available hollow-fiber PDMSXA1000 membrane module (Permselect©, MedArray Inc., USA), whose key geometric measurements are summarized in Table 2. A smaller version of this module was used for similar experimental validation in Henares et al. [7]. The gases of interest ($H_2$ or $CH_4$, or a mix of $H_2$ and $CH_4$) were bubbled into the CSTR reactor through an air stone. Rotameters were used to ensure the same gas bubbling rates between experiments. The water in the CSTR was recirculated using a peristaltic pump and a flow dampener. A flowmeter (Blue White Micro-Flo, FS1-201-4V, ±5% accuracy in experimental range) was used to determine the volumetric flowrate of liquid flowing through the membrane. The fluid was pumped through the lumen side of the membrane and returned to the CSTR. A 3-way valve was placed before and after the membrane for dissolved gas measurement.

A second peristaltic pump was used to pull vacuum on the shell-side of the membrane. A pressure indicator (WINTERS Vacuum Gauge, PFQ700LF, ± 1 kPa) was used to measure the vacuum pressure. The permeate was then pumped to a volumetric gas measurement system based on a water-displacement method. A 3-way valve was also attached on the permeate line to allow for permeate gas concentration measurements.

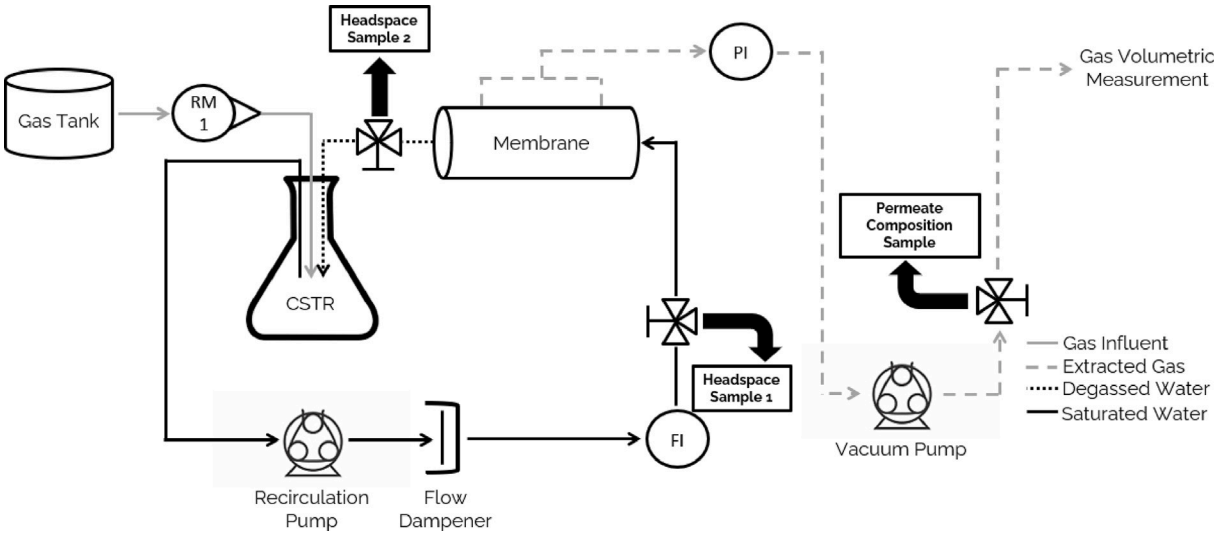


**Fig. 4.** Diagram of the experimental setup to determine gas recovery from pure water. For mixed-gases, two gas tanks and two rotameters were employed and combined into one line for addition to the CSTR. RM indicates a rotameter, PI indicate a pressure indicator, and FI indicates a flow indicator.

**Table 2**
Geometric measurements of the PDMS module used in the experiments.

| | |
|---|---|
| Fiber inner diameter [D] | 190 μm |
| Fiber outer diameter | 300 μm |
| Effective length [L] | 8.42 cm |
| Number of fibers | 1512 |
| Shell tube inner diameter | 1.89 cm |

**Table 3**
Root mean square (RMS) error between the model predicted $O_2$ extraction rates and the PDMSXA1000 data sheet using various Sherwood number correlations.

| Correlation | RMSE [%] |
|---|---|
| Leveque, Average Gz. | 4.51 |
| Newman, Average Gz. | 12.98 |
| Leveque, Local Gz. | 7.52 |
| Newman, Local Gz. | 7.49 |

The reactor was allowed to reach steady-state prior to taking dissolved gas samples for measurement. Steady-state was ensured by collecting a 200 μL sample of the permeate and testing the sample composition. When the permeate composition varied less than 5% over 3 measurements, it was assumed that steady-state had been reached.

The liquid headspace gas measurement was performed as follows. A syringe was attached to the 3-way valve to collect a liquid sample, 5 mL of which was inserted into an 11.5 mL crimp-top vial filled with argon gas. During the transfer of liquid from the syringe to the vial, a second syringe was inserted into the vial to keep the pressure in the system at 1 atm. The sample was then left to equilibrate at room temperature. The vial was shaken vigorously prior to headspace gas composition measurement. Permeate and headspace gas composition were determined using a gas chromatograph (GC, HP 6890 Series, with Supelco 45/60 Mol Sieve 13X column) equipped with a thermal conductivity detector (TCD) and argon reference gas.

The volume of recovered gas was measured via a liquid displacement method using an inverted graduated cylinder in water. The graduations on the cylinder were 10 mL for $H_2$ experiments, and 2 mL for $CH_4$ and mixed $H_2$-$CH_4$ experiments. Permeate samples were obtained through a 3-way stopcock capped with a rubber septum. It was assumed that a negligible amount of air was present in the permeate at steady-state. This was due to the vigorous bubbling of gas into the CSTR, which inhibited air diffusion into the water.

### 3.2. Experimental design

Steady-state gas recovery experiments were performed in a $3^2$ design of experiments (DOE) with a center point. Vacuum pressure was varied from −60 kPa to −80 kPa, operating temperature from 20 °C to 40 °C, and linear flow velocity from 9 to 18 cm/s. The center point operating condition was −70 kPa vacuum pressure, 30 °C, and a linear flow velocity of 14 cm/s. Pure $H_2$ recovery experiments were performed as a full-factorial DOE. However, $CH_4$ and mixed $H_2$-$CH_4$ experiments were performed as a partial-factorial DOE, where experiments were selected according to latin hypercube sampling methods.

The steady-state gas recovery experiments were performed in at least duplicates. Samples for dissolved gas measurement were taken in duplicates.

The gas flowrate into the CSTR for single-gas experiments was set at 5 SCFH-air for $H_2$ experiments, and either 5 or 10 SCFH-air for $CH_4$ experiments, which were the highest bubbling rates that could be achieved without overflowing the CSTR. For simultaneous permeation of $H_2$ and $CH_4$, a second rotameter was utilized to allow the flowrates of both gases to be controlled separately. The gas flowrate was set at 2.5 SCFH-air of $H_2$ and 10 SCFH-air of $CH_4$ for mixed gas experiments.

## 4. Results and discussion

### 4.1. Single gas permeation

The model was first compared to the data published by Permselect© for the PDMSXA1000 membrane. Data was provided for the deoxygenation of water, where the feed water had 8.0 mg/L $O_2$. The deoxygenation process used a 10 Torr vacuum to drive permeation, and used flowrates between 50–800 mL/min (linear flow velocities of 2.30–36.74 cm/s) at 23 °C. The model was run for 10 min with $n = 250$ segments, and solved using the BDF solver in the scipy Python library. Independency with respect to time and number of segments was confirmed. We assumed a saturated $N_2$ concentration in the feed, and the presence of water vapor permeation.

Good agreement between the model and the published deoxygenation data was observed while using Eq. (3) with the averaged Graetz number (Fig. 5), despite the significant development of the mass transfer boundary layer (Table 3). Therefore, the averaged Graetz number was used for the simulations.

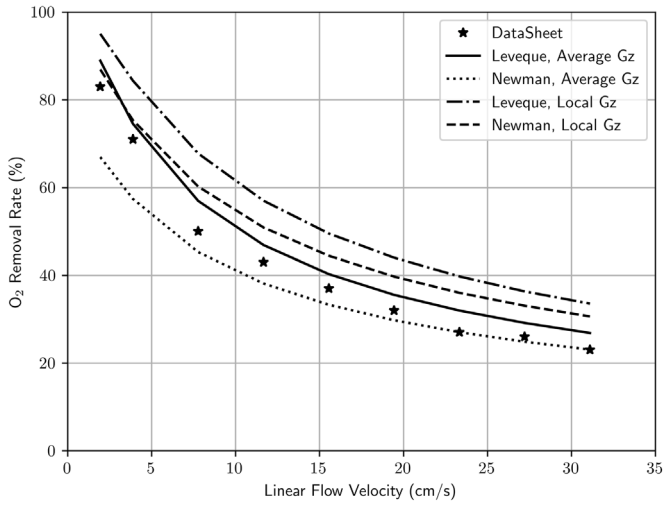


**Fig. 5.** Model results for $O_2$ and $N_2$ diffusion from a PDMSXA-1000 membrane contactor compared to the membrane manufacturer datasheet. The comparisons show both the Leveque and Newman correlations using Local and Average Graetz numbers. The plot shows that the Leveque correlation using the average Graetz number resulted in the most accurate prediction.

Although Wickramasinghe et al. warned that the assumptions implicit in the Leveque approximation and the Newman extension are no longer valid "when the diffusion boundary layer reaches the center of the tube", it has also been shown that the approximation and the extension are able to accurately predict the Sherwood numbers from experimental data [26,31,33,34]. Due to the rich body of research that has verified the Leveque approximation, and therefore the corresponding Newman extension, for hollow fibers, we chose to use Eq. (4) to approximate the liquid-side mass transfer coefficient.

The model was then compared to data from the experimental setup described in Section 3.1 using $H_2$ and $CH_4$ gases. The model predicted $H_2$ extraction with an average absolute error of 10%, and $CH_4$ extraction with an average absolute error of 13% (Fig. 6). The slope of the linear regression lines were 0.92 and 1.09 for $H_2$ and $CH_4$ respectively, where parity with the model would result in a slope equal to one.

It was assumed that the permeate composition contained negligible amounts of air. GC measurements determined that the average permeate air composition was 3%. This assumption could account for the model's underestimation of gas extraction rates, because the presence of air in the permeate would increase the permeation rate of $H_2$ and $CH_4$.

Additionally, diffusion coefficients of pure gases in water can differ significantly between sources. For $H_2$, diffusion coefficients were fitted from both Verhallen et al. and the CRC Handbook, resulting in Wilke-Chang association parameters of 8.4 and 9.84, respectively [42,48]. For $CH_4$, diffusion coefficients were fitted from both Witherspoon et al. and the CRC Handbook, resulting in Wilke-Chang association parameters of 1.8 and 2.2, respectively [42,43]. Meanwhile, the original Wilke-Chang correlation suggests an association parameter of 2.6 for $CH_4$. We used an association parameter of 9.84 for $H_2$ and 2.2 for $CH_4$, corresponding with data from the most recent source. Generally gas extraction rates will increase with diffusion coefficients. Therefore, an overprediction of gas extraction rates could imply that the diffusion coefficient of that gas is too high, and vice versa. It is noted that pure hydrogen recovery rates are generally underestimated, while pure methane recovery rates are generally overestimated. We have compared the errors at different operating conditions, and found no consistent trends.

Given that the model did not use empirical parameters outside of published results for diffusion coefficients of gases, an average error of 13% is thought to be acceptable and provides sufficient confidence for the parametric analysis described below.

### 4.2. Multiple gas permeation

Due to the lower bubbling rate of both $CH_4$ and $H_2$ in the mixed-gas experiments, the extraction rates of both gases were much lower compared to their single-gas equivalents (Fig. 6). $H_2$ was extracted at a rate of 0.5–1.0 mL/min as opposed to 1.5–3.2 mL/min, while $CH_4$ was extracted at a rate of 1.0–2.0 mL/min as opposed to 1.8–3.5 mL/min. The lower bubbling rates are due to a limitation in our experimental apparatus, where we cannot bubble more gas into our tank, or else it will overflow. Additionally, these higher bubbling rates could result in gas bubbles in the hollow-fiber membranes, further skewing the results.

The lower gas extraction rates also led to increased error relative to the single-gas permeation results, especially for $H_2$ extraction. The average error of the mixed gas extraction data was initially 22%. A significantly higher percentage of $N_2$ in the permeate, however, was observed. In the case of single-gas measurements, the majority of experiments showed no $N_2$ presence, with an average of 3 mol% $N_2$. In the case of mixed-gas permeation, the majority of the experiments showed $>$ 5 mol% $N_2$, with a maximum of 18 mol% $N_2$ and an average of 6 mol% $N_2$. Additionally, none of the experiments showed a complete absence (0 mol%) of $N_2$. This suggests that the initial assumptions were no longer valid. Therefore, the model data shown in Fig. 6 for mixed-gas extraction included a 10% saturation of $O_2$ and $N_2$ (0.91 mg/L and 1.45 mg/L, respectively) in the feed water. This reduced the average absolute error for $H_2$ and $CH_4$ extraction rates to 16%. Additionally, this resulted in an average $N_2$ concentration of 6 mol%, which agreed with the experimental average $N_2$ permeate concentration. The addition of the 10% saturation of $O_2$ and $N_2$ resulted in an $R^2$ value of 0.98 and a slope of 0.96.

Averaging between the single-gas and multiple-gas comparisons between modeled and experimental gas extraction rates resulted a slope of 1.02, an $R^2$ value of 0.98, an average error of −1%, and an average absolute error of 13%. The model was predictive of the variation of gas extraction rates from 0.5 mL/min to 3.5 mL/min.

### 4.3. Model validation with published data

In addition to comparing the model with experimental values collected for this study, the model was also compared with experimental gas extraction efficiencies (Eq. (11)) described in the literature, including the removal of $O_2$ from air-saturated water [26,49] and the removal of $CH_4$ from anaerobic digester effluent [7]. The operating parameter ranges are shown in Table 4. The results showed an average error of -9% and an average absolute error of 11% (Fig. 7).

$$\mathrm{RE}_i\ [\%] = \frac{C_{i,in} - C_{i,out}}{C_{i,in}} \tag{11}$$

The fit with respect to other published values was more difficult to analyze as a result of uncertainties in membrane geometries and operating parameters. In the case of Henares et al. the inlet $CO_2$ concentration was not reported, and so it was assumed that the biogas concentration was in equilibrium with the $CO_2$ concentration in the wastewater [7].

In the case of Ito et al. the reported effective membrane area did not agree with the calculated membrane area based on reported effective length, membrane inner diameter, and number of fibers [49]; the calculated value was used.

Despite the addition of these potential error or data limitations, the model comparison resulted in an $R^2$ value of 0.96, indicating that the model was predictive of 96% of the variation between the experimental data points.

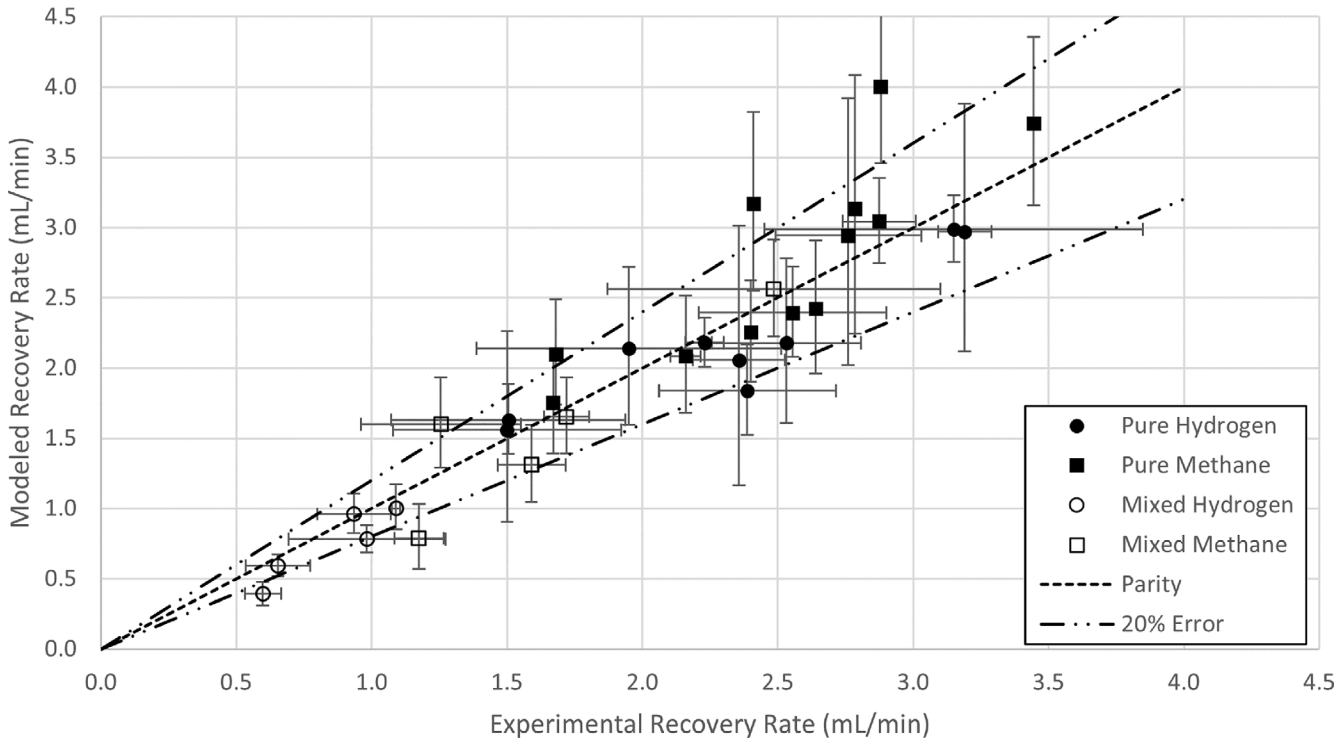


**Fig. 6.** Comparison between the experimental gas extraction rate and the modeled gas extraction rates. The dashed line indicates the location of the experimental data points that match the modeled extraction rates, while the dashed-dot line indicates 20% prediction error. X-error bars represent the standard deviation between experimental extraction rate data, while Y-error bars represent the error in modeled extraction rates due to errors in dissolved gas concentration from GC measurements.

**Table 4**
Operating parameter ranges for published data comparisons.

| Paper | Linear flow velocity (cm/s) | Temperature (K) | Vacuum pressure (-kPa) |
|---|---|---|---|
| Henares et al. [7] | 1.2–32.7 | 298.15 | 14–80 |
| Tan et al. [26] | 4.4–17.7 | 295 | 97 |
| Ito et al. [49] | 53 | 293.15–295.15 | 50–100 |

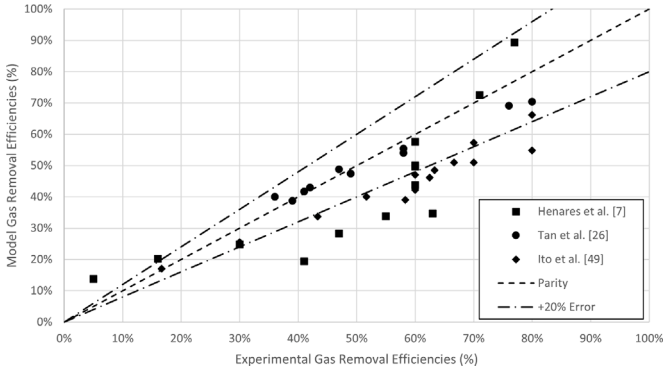


**Fig. 7.** Comparison of the model predicted gas removal efficiencies of $O_2$ [26,49] and $CH_4$ [7], with an average error of −9% and an average absolute error of 11%.

### 4.4. Model parametric analysis

After experimental validation of both single-gas extraction and mixed-gas extraction, the model was used to parametrically analyze the effects of vacuum pressure, linear flow velocity, and water temperature on the extraction rates of $H_2$ and $CH_4$ from a mixed feed. The model used a steady-state feed that was fully saturated by both $H_2$ and $CH_4$ (1.6 mg/L and 21 mg/L, respectively) and starved of air. To model a step change in feed concentrations, shell-side initial conditions were that of air at the vacuum pressure.

Fig. 8a shows the effect of vacuum pressure and linear flow velocity on the extraction rate of $H_2$ at temperatures of 20, 30, and 40 °C. The modeled extraction rate increased with temperature, vacuum pressure, and flow velocity. Fig. 8a also shows that the effect of increasing vacuum pressure on gas extraction rate differed based on other operating conditions. Specifically, lowering the vacuum pressure from −50 kPa to −90 kPa at 3.9 cm/s and 20 °C resulted in a 23% increase in gas extraction rate, but at 40 °C, the same vacuum pressure increase only resulted in a 15% increase in gas extraction rate.

Fig. 8b shows the effect of vacuum pressure and linear flow velocity on the removal efficiency of $H_2$ at the same temperatures. The model again followed the expected trends of a hollow fiber gas extraction unit, where an increase in linear flow velocity decreased the gas removal efficiency as a result of a decrease in hydraulic residence time. Increases in vacuum pressure and temperature, however, both increased removal efficiency as a result of an increase in the mass transfer driving force and the gas diffusion coefficients, respectively.

An interesting phenomena that our model highlighted is a change in the effect of vacuum pressure on extracted gas composition. Fig. 9 shows the ratio of $H_2$ and $CH_4$ gas in the extracted gas stream at different temperatures and membrane lengths. Under various combinations

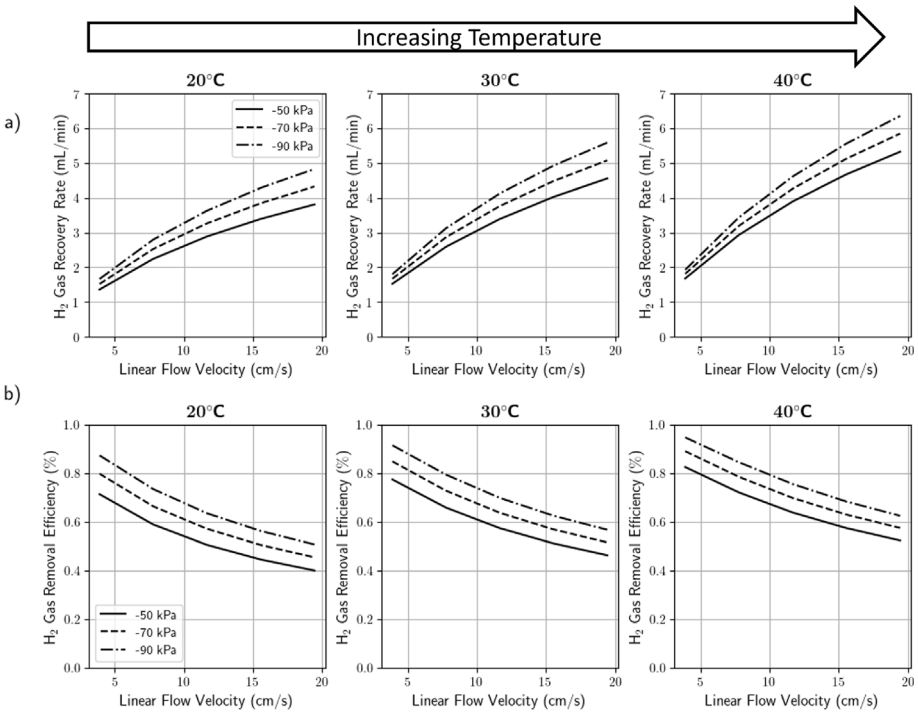


**Fig. 8.** Parametric analysis of multi-component gas extraction with a steady-state water feed saturated with both $H_2$ and $CH_4$. The figure shows the effects of linear flow velocity, temperature, and vacuum pressure on the (a) $H_2$ extraction rate, and (b) $H_2$ removal efficiency.

of membrane length and temperature, there exists a linear flow velocity under which lowering vacuum pressure decreases $H_2$ mol % in the permeate, but above which lowering vacuum pressure increases $H_2$ mol % in the permeate. Specifically, these cross-over points appear in the middle-left, center, bottom-left, and bottom-middle plots.

This phenomena occurs as a result of a changing balance between the retention time and the gas driving forces. Fig. 9 shows that increased membrane length (and therefore retention time) shifts the critical linear velocity up.

Combining the linear flow velocity and membrane length variables into hydraulic residence time (HRT) – the average time the feed stays inside the fibers – shows a clearer picture of the physical phenomena responsible for the reversal of the effect of vacuum pressure on gas recovery ratio (Fig. 10). Specifically, if the retention time was short, and the temperature was sufficiently high, a higher vacuum pressure selected for the gas with the higher total mass transfer coefficient, which in this case was $H_2$. As retention time increases, more of the other gaseous components were recovered when the vacuum pressure was increased, thus reducing the recovery ratio. When the retention times were short, kinetic effects dominated.

## 5. Conclusion

A first-principles model for gas recovery from water using a side stream hollow-fiber membrane module was developed and validated both experimentally for the recovery of $H_2$, $CH_4$ and a mixture of $H_2$ and $CH_4$, and against published literature data. During model development, it was found that despite the theoretical presence of a significant mass-transfer boundary layer in the hollow-fiber membranes, the classical Leveque solution best described the liquid mass transfer process. Additionally, the averaged Graetz number was found to be a better estimate of the liquid mass transfer coefficient compared to using a local Graetz number. Therefore, despite the assumptions implicit in the Leveque approximation, it still serves as a sufficient way to estimate the liquid mass transfer coefficient.

Experimental validation shows that the model had good predictive capability for gas recovery from pure water, with an average absolute error of 10%–16% in lab-scale gas recovery experiments, and 11% when compared against published data from the literature. Additionally, the model was predictive of 98% of the variation of removal efficiencies from lab-scale testing, and 96% of the variation of removal efficiencies from published data sets. The model-predicted effects of operating parameters on gas recovery rates agreed with engineering intuition. Parametric analysis also revealed coupled effects that were not immediately clear from basic engineering principles. These trade-offs will be important in designing gas recovery systems, particularly for two-stage AD processes.

One limitation of the presented experimental validation was the inability to completely remove air from the liquid feed. Future gas recovery experiments should be performed in such a way as to remove the need for this assumption, and such that validation of transient effects can be performed.

## Declaration of competing interest

The authors declare that they have no known competing financial interests or personal relationships that could have appeared to influence the work reported in this paper.

## Data availability

Data will be made available on request.

## Acknowledgments

This work was supported by the 3M Science and Technology Graduate Fellowship, United States, and by the Industrial Decarbonization Offices of the U.S. Department of Energy under award number DE-EE0009501.

We also acknowledge Dr. Jeremy Guest and Dr. Xinyi Zhang from the University of Illinois at Urbana-Champaign for helpful discussions in the development of the model.

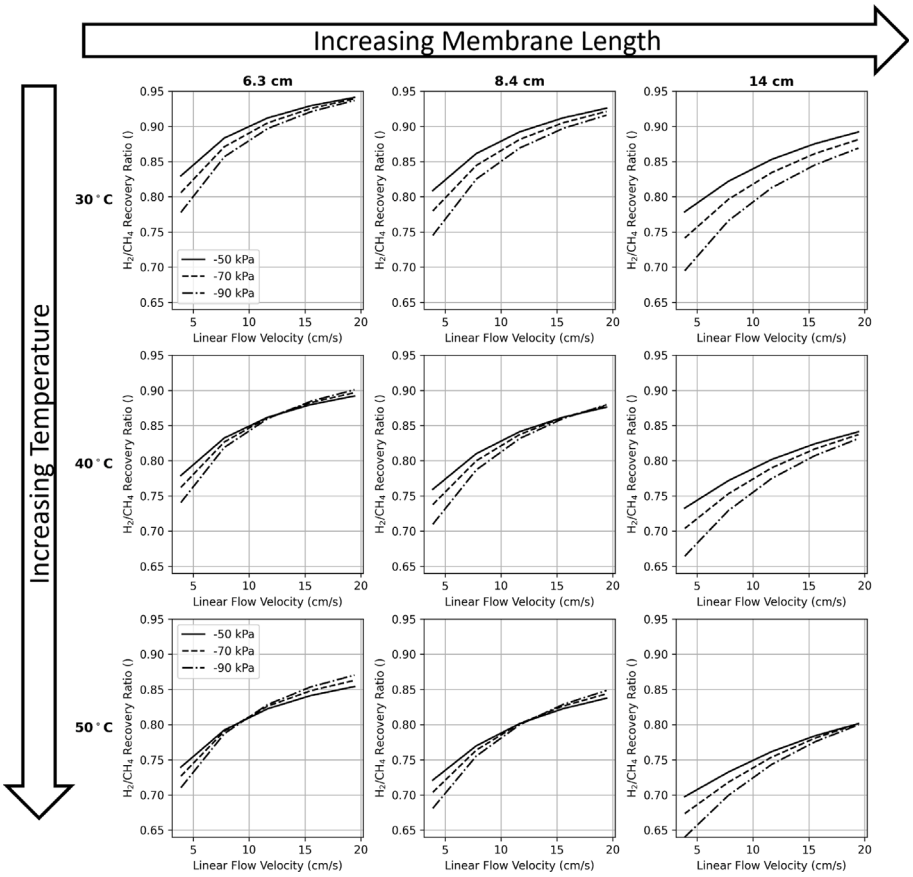


**Fig. 9.** Parametric analysis of $H_2/CH_4$ gas recovery ratio as a function of membrane length, linear flow velocity, temperature, and vacuum pressure.

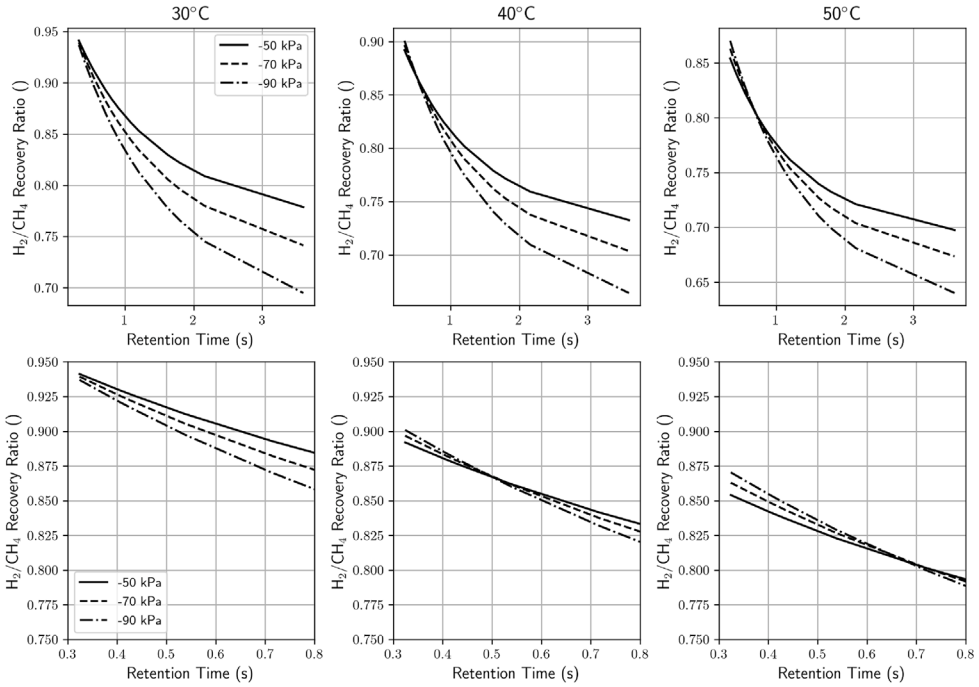


**Fig. 10.** Parametric analysis of $H_2/CH_4$ gas recovery ratio as a function of hydraulic residence time, temperature, and vacuum pressure.

## Appendix A. Temperature dependence of gas properties

Below are enumerated the equations described in Section 2.3.1 for clarity.

a. The equation for the absolute viscosity of water that was fitted by Huber, et al. is shown below [39]. The viscosity is in units of Pa s.

$$\mu = (1\times10^{-6})\left(a\left(\frac{T}{T_{\text{ref}}}\right)^{-1.9} + b\left(\frac{T}{T_{\text{ref}}}\right)^{-7.7} + c\left(\frac{T}{T_{\text{ref}}}\right)^{-19.6} + d\left(\frac{T}{T_{\text{ref}}}\right)^{-40.0}\right) \tag{12}$$

where:

$$a = 280.68, \quad b = 511.45, \quad c = 61.131, \quad d = 0.45903, \quad T_{\text{ref}} = 300\ \text{K}$$

b. The equation for liquid density of water as a function of temperature found from the AIChE DIPPR Database, Equation # 100 is shown below. The density calculated is in units of kg/m$^3$.

$$\rho = 18 * (-13.851 + 0.64038 * T - 1.9124\times10^{-3}T^2 + 1.8211\times10^{-6}T^3) \tag{13}$$

c. The equation for Henry's Law Coefficients for Henry's Law Coefficient is found in the NIST Webbook in the following general form:

$$k_H(T) = k_H^{\circ}\exp\left(\frac{d(\ln k_H)}{d(1/T)}\left(\frac{1}{T} - \frac{1}{298.15}\right)\right) \tag{14}$$

The values used for $k_H^{\circ}$ (standard Henry's Law coefficient at 298.15 K) and $\frac{d(\ln k_H)}{d(1/T)}$ (the temperature dependency coefficient) used for each gas is shown below in Table 5.

## Appendix B. Wilke-Chang association parameters

To determine the appropriate Wilke-Change association parameter for the gases of interest ($H_2$, $CH_4$, $O_2$, and $N_2$), we fitted the Wilke-Chang correlation shown in Eq. (9) by plotting the diffusion of gas $j$ in $H_2O$, $D_{j,H_2O}$ against the function of temperature $T$. In other words, we can re-write Eq. (9) as:

$$D_{j,H_2O} = \phi F(T) = \phi\left(\frac{(7.4\times10^{-8})(\text{MW}_{H_2O})^{0.5}}{\mu\bar{V}_j}T\right) \tag{15}$$

The viscosity of water as a function of temperature $\mu$ can be found using the equation from Huber, et al. reproduced in Eq. (12) [39]. The molar volume at normal boiling point $\bar{V}_j$ can be calculated using Eq. (10), where the critical molar volumes of each gas are shown below (Table 6).

The diffusion coefficients were then plotted against $F(T)$, and the slope taken to determine the appropriate association parameter $\phi$ (see Table 7).

**Table 5**
Table of constants used for each gas for Henry's Law coefficient determination. These have been converted from the ones shown in the NIST website by converting the coefficients to units of mol/Pa m$^3$.

| Gas | $k_H^{\circ}$ [mol/Pa m$^3$] | $\frac{d(\ln k_H)}{d(1/T)}$ |
|---|---|---|
| $H_2$ | $7.8\times10^{-6}$ | 640 |
| $CH_4$ | $1.3\times10^{-5}$ | 1900 |
| $O_2$ | $12\times10^{-6}$ | 1800 |
| $N_2$ | $6\times10^{-6}$ | 1300 |

**Table 6**
Critical molar volumes as retrieved from the NIST Webbook.

| Gas | $V_C$ [cm$^3$/mol] |
|---|---|
| $H_2$ | 64.15 |
| $CH_4$ | 98.6 |
| $O_2$ | 73.4 |
| $N_2$ | 89.21 |

**Table 7**
Association parameters based on a linear regression of various data sets against Eq. (15), and the appropriate temperature ranges of the experiments.

| Gas | T range [K] | $\phi$ | $R^2$ | Data source |
|---|---|---|---|---|
| $H_2$ | 283–308 | 9.84 | 0.9985 | [41] |
| $CH_4$ | 283–308 | 2.2 | 0.9998 | [41] |
| $O_2$ | 275–333 | 1.9 | 0.9967 | [45] |
| $N_2$ | 293–360 | 1.77 | 0.9960 | [46] |

## Appendix C. Model sensitivity analysis

Aside from the model parametric analysis performed in Section 4.4, we performed a one-at-a-time (OAT) sensitivity analysis. OAT analysis refers to a simple process in which first-order effects of various parameters on model outputs are determined. We first determine a set of baseline parameters, and then change the parameters one at a time to determine the effects of the changing parameter on the model output.

We define a gas recovery system where the input flow is saturated with $H_2$ (1.6 mg/L), $O_2$ (8.6 mg/L), and $N_2$ (13.8 mg/L). The baseline model uses the following operating parameters: temperature of 20° C, vacuum pressure of −80 kPa, volumetric flowrate of 300 mL/min, $H_2$ and $O_2$ diffusion and permeability coefficients as determined by the Wilke-Chang equation (Appendix B) and the Permselect datasheet [32] respectively. The membrane geometric properties are set at an effective length of 8.41 cm, and a membrane area of 0.12 m$^2$. The fibers used are consistent with an inner diameter of 190 um and an outer diameter of 300 um.

The objective of this sensitivity analysis is to determine the effects of:

- Gas recovery operating parameters (temperature, vacuum pressure, and flowrate)
- Physical properties of the primary target gas ($H_2$) and an unintended gas ($O_2$) in water and the membrane
- Membrane geometry

on the primary outputs of the model:

- Recovery rate of our primary gas target ($H_2$)
- Total removal percentage of our primary gas target ($H_2$)
- Total gas recovery rate (a measure of primary gas purity)
- Recovery rate of our unintended gas ($O_2$) that will reduce the purity of our product

It was found that within the operating range of the model (between 20 and 40 °C for AD systems), the effects of temperature on the recovery rate of both the primary and unintended gases are linear (Fig. 11). This is likely due to the combined effects of multiple factors, including the non-linear effects of temperature on gas diffusivity in water, vapor pressure of water, and the relatively small changes in temperature. Additionally, we see that increasing the operating temperature increases the recovery rate and removal percentage of each gas, since increasing temperature generally increases rates of mass transport.

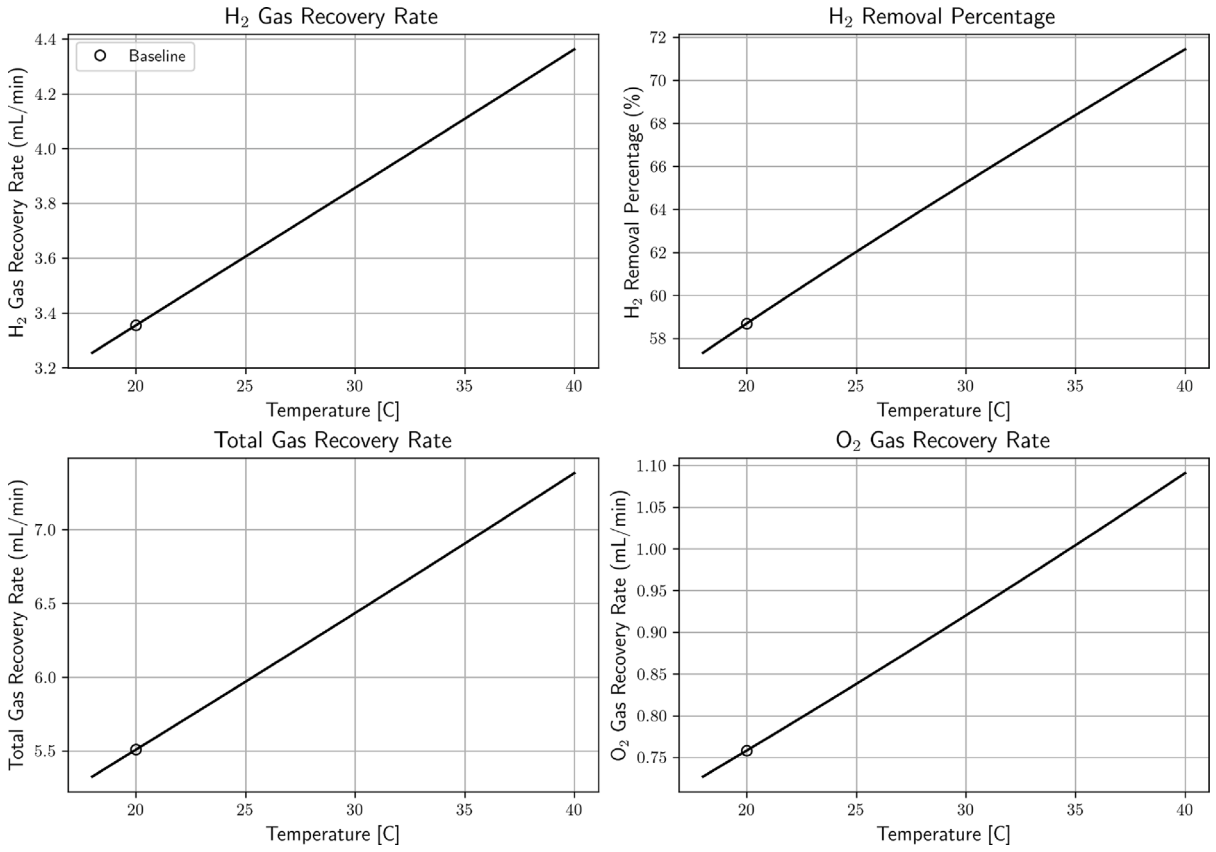


**Fig. 11.** OAT analysis on the effects of the operating temperature.

Similar to temperature, we see that decreasing the operating vacuum pressure increases the gas recovery rate of all gases due to the increased driving force (Fig. 12). This agrees with fundamental transport phenomena.

The effects of linear flow velocity on the recovery of gases show that increasing linear flow velocity increases the gas recovery rates of both primary and unintended gases, simply due to the increase of water that is being degassed (Fig. 13). However, we see that the removal percentage decreases due to the reduction in hydraulic residence time, which also follows our understanding of fundamental transport phenomena.

The effects of the primary gas diffusivity (Fig. 14) and membrane permeability (Fig. 15) on the recovery rate is very clearly non-linear. Specifically, it is noteworthy to see that the gas recovery rate and removal percentage ranges when scaling the gas diffusivity by a factor of 10 can change the removal percentage by factors of 2-3. Although the non-linear trend is also seen in the effects of membrane permeability, the difference in y-axes ranges clearly show that increasing diffusivity has a greater effect on $H_2$ gas recovery rates and removal percentages compared to the membrane permeability. This echoes some of the conclusions Elimelech and Phillip reported on the limits of membrane permeability on the separation capabilities of membrane technologies, and why other effects – such as liquid hydrodynamics – should be the focus instead of the membrane material [50].

We see much of the similar trends as we described above in Figs. 16 and 17 for the effects of $O_2$ diffusivity and permeability on gas recovery rates. Their effects on the primary gas recovery, though, is very small.

The effects of membrane geometry also follow our understanding of fundamental membrane transport. Specifically, we see that the length of the fiber makes very little difference in our recovery results, provided that the membrane area is constant (Fig. 18). This is consistent with many of our bulk membrane module modeling equations, where the characteristic parameter is the membrane area, not the membrane length. Similarly, we see that an increase in membrane area (Fig. 19) — which in this case corresponds with increasing the number of hollow fibers — will significantly increase gas recovery rates.

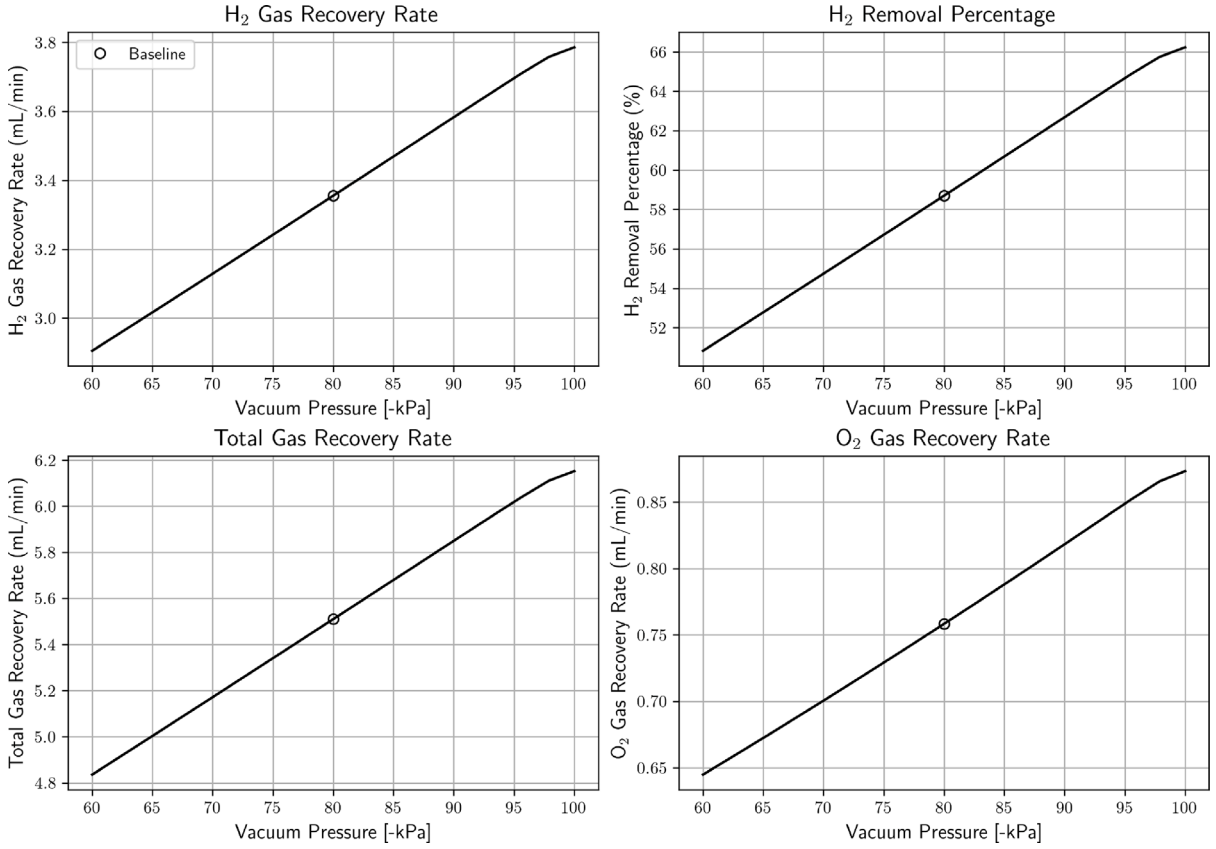


**Fig. 12.** OAT analysis on the effects of the operating vacuum pressure.

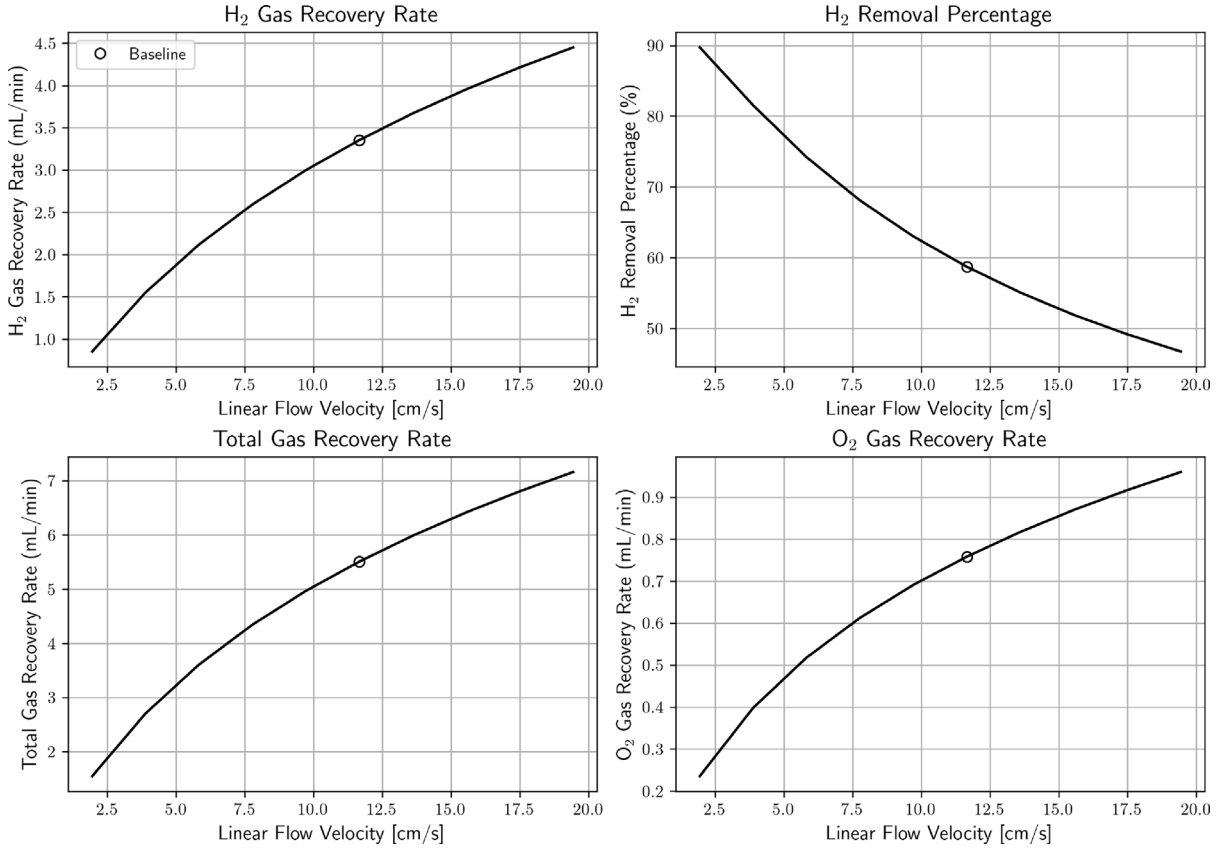


**Fig. 13.** OAT analysis on the effects of the operating linear flow velocity.

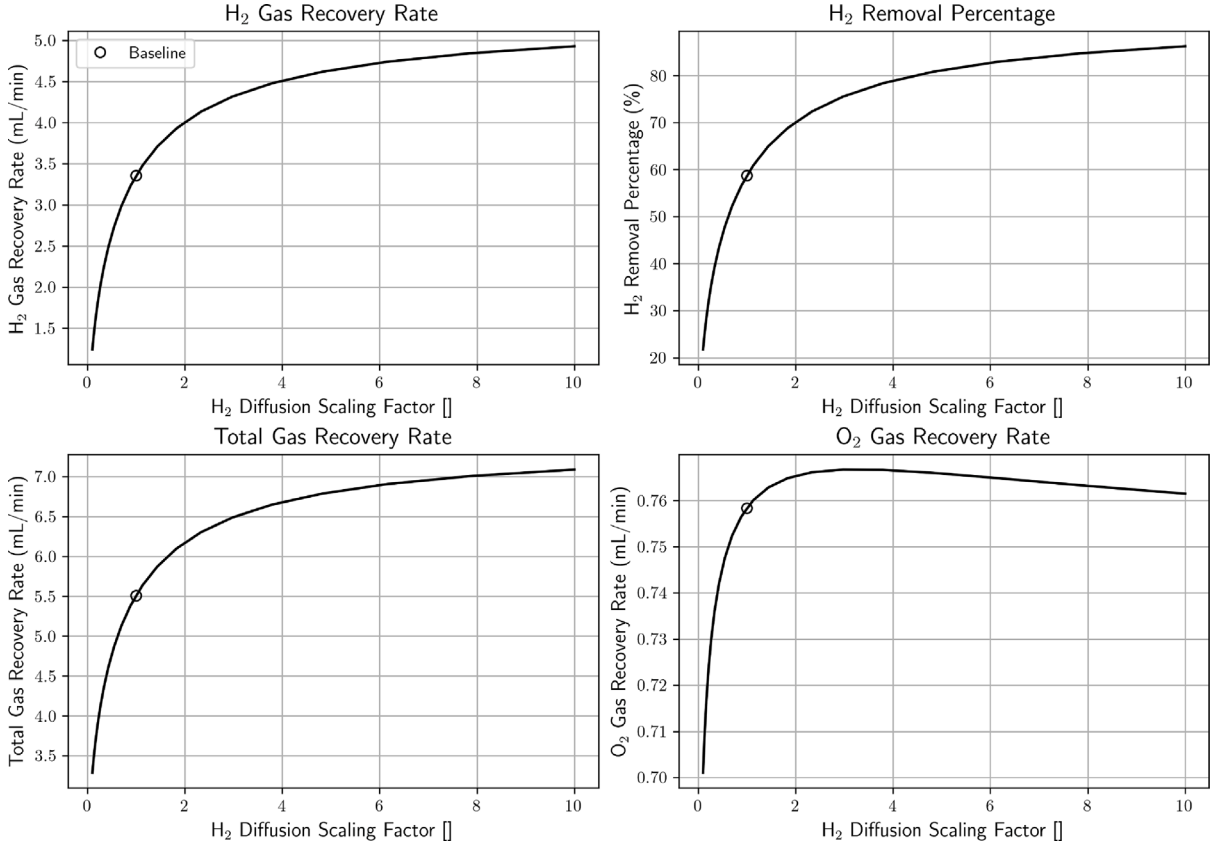


**Fig. 14.** OAT analysis on the effects of the primary gas ($H_2$) diffusivity in water.

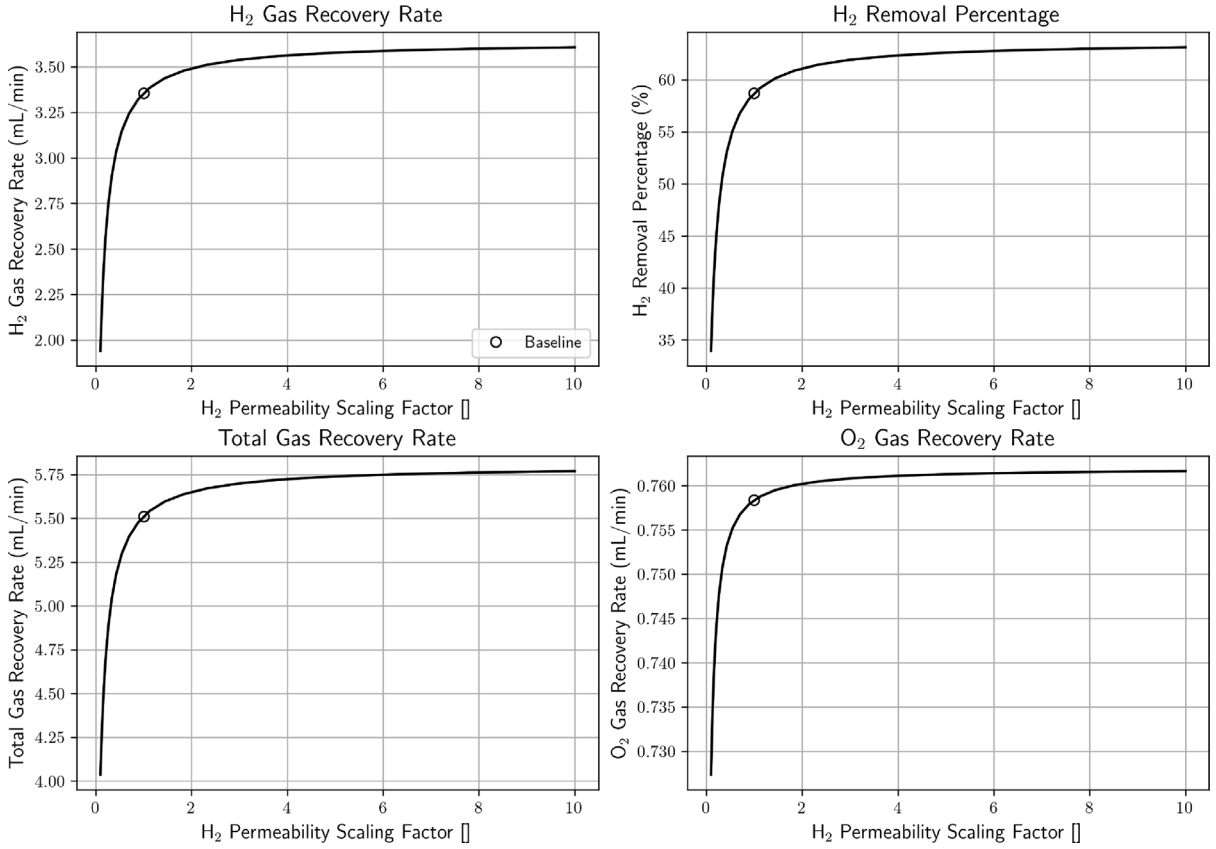


**Fig. 15.** OAT analysis on the effects of the primary gas ($H_2$) permeability through the membrane.

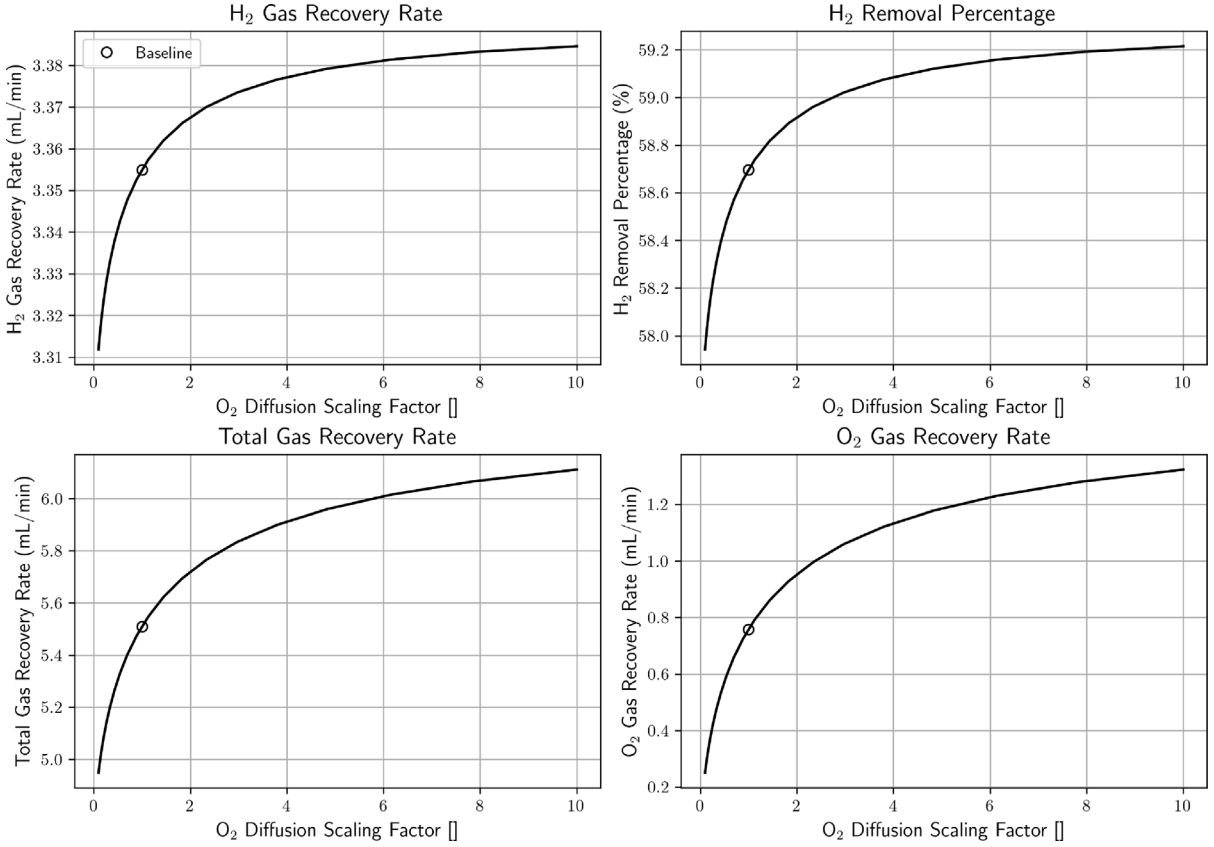


**Fig. 16.** OAT analysis on the effects of the unintended gas ($O_2$) diffusivity in water.

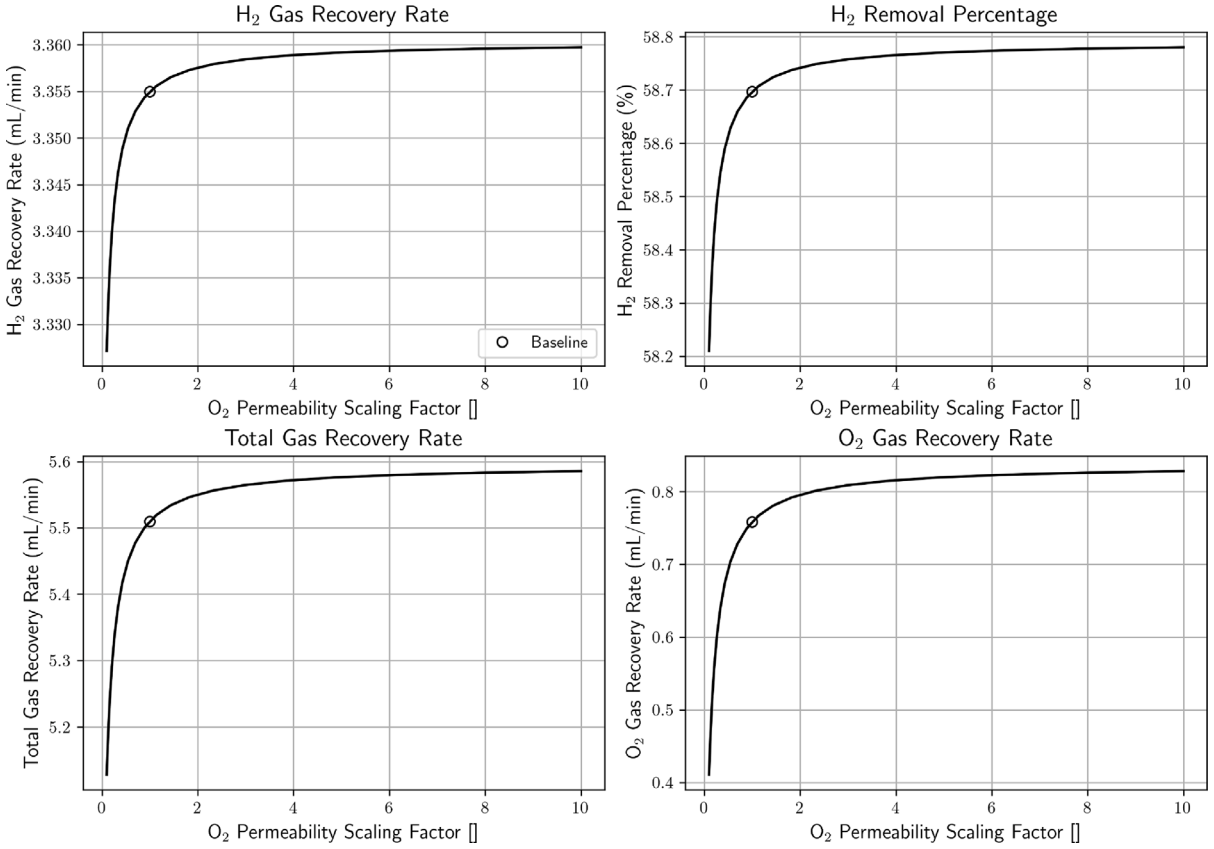


**Fig. 17.** OAT analysis on the effects of the unintended gas ($O_2$) permeability through the membrane.

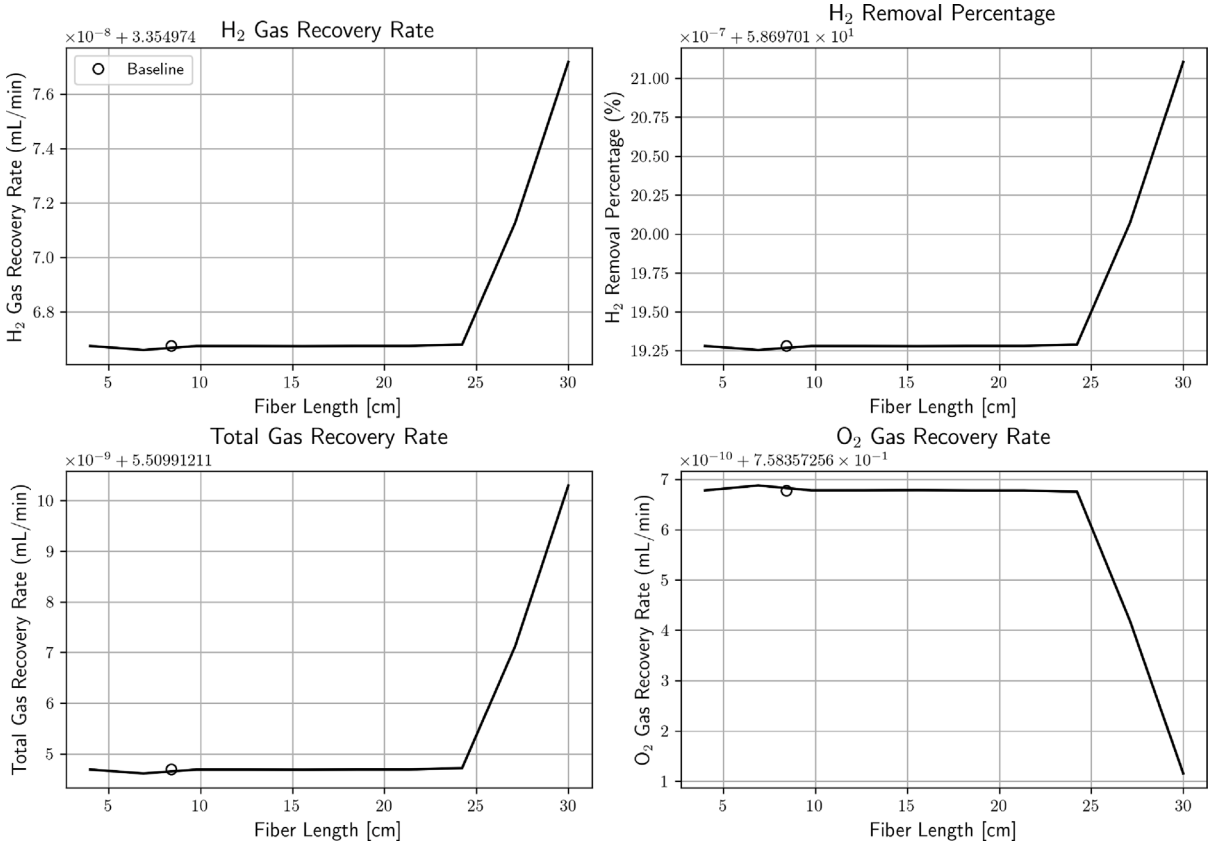


**Fig. 18.** OAT analysis on the effects of the fiber length, keeping total membrane area constant, but changing the number of tubes.

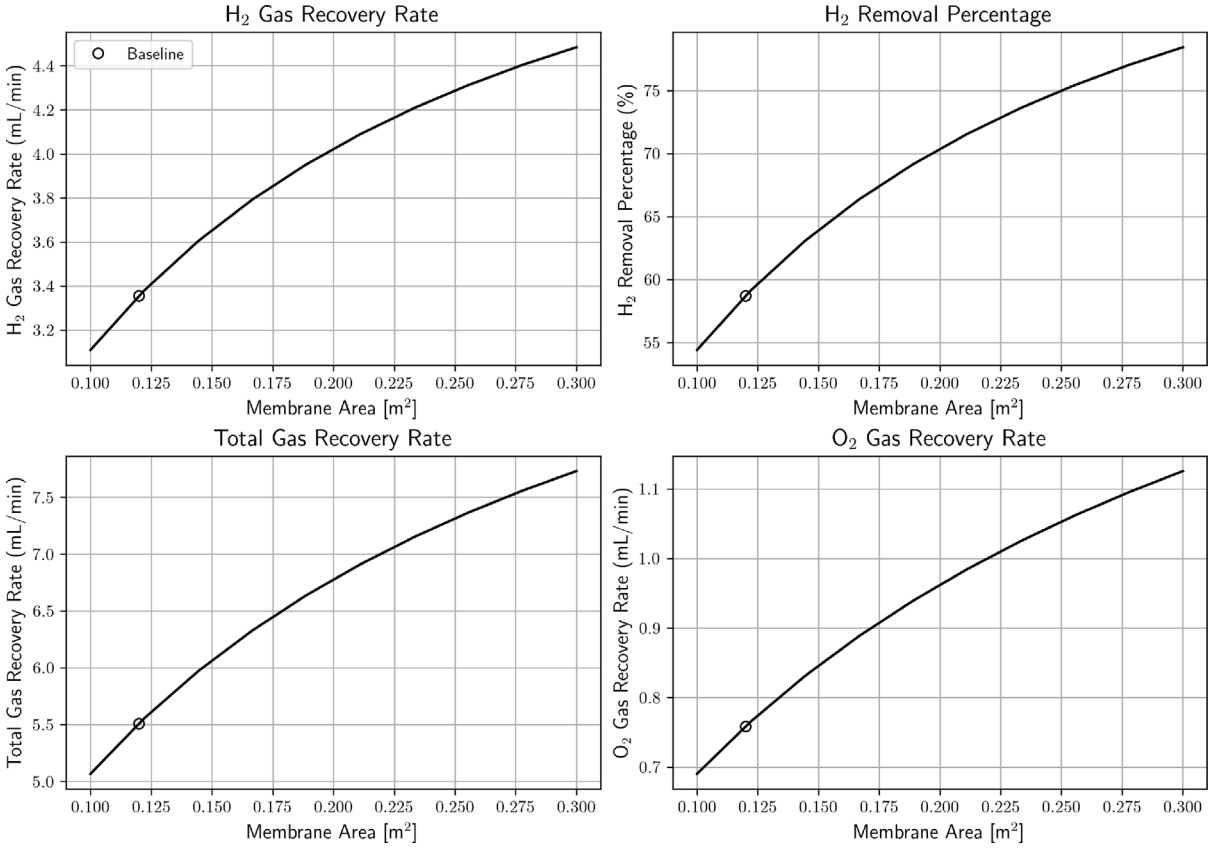


**Fig. 19.** OAT analysis on the effects of the membrane area, keeping membrane length constant, but changing the number of tubes.

## References


[1] International Energy Agency (IEA), World energy outlook 2016 excerpt water energy nexus, 2016, p. 63.
[2] International Energy Agency (IEA), World energy outlook 2018, 2018, p. 661.
[3] United Nations, Transforming our world: The 2030 agenda for sustainable development, 2015.
[4] J. Cookney, A. Mcleod, V. Mathioudakis, P. Ncube, A. Soares, B. Jefferson, E. McAdam, Dissolved methane recovery from anaerobic effluents using hollow fibre membrane contactors, J. Membr. Sci. 502 (2016) 141–150.
[5] W.M. Bandara, H. Satoh, M. Sasakawa, Y. Nakahara, M. Takahashi, S. Okabe, Removal of residual dissolved methane gas in an upflow anaerobic sludge blanket reactor treating low-strength wastewater at low temperature with degassing membrane, Water Res. 45 (11) (2011) 3533–3540.
[6] W. Rongwong, S. Wongchitphimon, K. Goh, R. Wang, T.-H. Bae, Transport properties of CO2 and CH4 in hollow fiber membrane contactor for the recovery of biogas from anaerobic membrane bioreactor effluent, J. Membr. Sci. 541 (2017) 62–72.
[7] M. Henares, M. Izquierdo, P. Marzal, V. Martínez-Soria, Demethanization of aqueous anaerobic effluents using a polydimethylsiloxane membrane module: Mass transfer, fouling and energy analysis, Sep. Purif. Technol. 186 (2017) 10–19.
[8] E. Centeno Mora, C.d.L. Chernicharo, Use of membrane contactors for removing and recovering dissolved methane from anaerobic reactors effluents: State-of-the-art, challenges, and perspectives, Rev. Environ. Sci. Bio/Technol. 19 (3) (2020) 673–697.
[9] P.L. McCarty, J. Bae, J. Kim, Domestic wastewater treatment as a net energy producer–can this be achieved? Environ. Sci. Technol. 45 (17) (2011) 7100–7106, Publisher: American Chemical Society.
[10] A. Schievano, A. Tenca, B. Scaglia, G. Merlino, A. Rizzi, D. Daffonchio, R. Oberti, F. Adani, Two-stage vs single-stage thermophilic anaerobic digestion: Comparison of energy production and biodegradation efficiencies, Environ. Sci. Technol. 46 (15) (2012) 8502–8510.
[11] R. Nabaterega, V. Kumar, S. Khoei, C. Eskicioglu, A review on two-stage anaerobic digestion options for optimizing municipal wastewater sludge treatment process, J. Environ. Chem. Eng. 9 (4) (2021) 105502.
[12] S. O-Thong, C. Mamimin, P. Prasertsan, S. O-Thong, C. Mamimin, P. Prasertsan, Biohythane Production from Organic Wastes by Two-Stage Anaerobic Fermentation Technology, Advances in Biofuels and Bioenergy, IntechOpen, 2018, Publication Title.
[13] S.A. Abdur Rawoof, P.S. Kumar, D.-V.N. Vo, T. Devaraj, S. Subramanian, Biohythane as a high potential fuel from anaerobic digestion of organic waste: A review, Renew. Sustain. Energy Rev. 152 (2021) 111700.
[14] D. Batstone, J. Keller, I. Angelidaki, S. Kalyuzhnyi, S. Pavlostathis, A. Rozzi, W. Sanders, H. Siegrist, V. Vavilin, The IWA anaerobic digestion model no 1 (ADM1), Water Sci. Technol. 45 (10) (2002) 65–73.
[15] P.A. Breach, S.P. Simonovic, Wastewater treatment energy recovery potential for adaptation to global change: An integrated assessment, Environ. Manag. 61 (4) (2018) 624–636.
[16] A. Berktay, B. Nas, Biogas production and utilization potential of wastewater treatment sludge, Energy Sources Part A: Recov. Util. Environ. Eff. 30 (2) (2007) 179–188, Publisher: Taylor & Francis _eprint:.
[17] S. Chen, B. Chen, Net energy production and emissions mitigation of domestic wastewater treatment system: A comparison of different biogas–sludge use alternatives, Bioresour. Technol. 144 (2013) 296–303.
[18] G. Silvestre, B. Fernández, A. Bonmatí, Significance of anaerobic digestion as a source of clean energy in wastewater treatment plants, Energy Convers. Manage. 101 (2015) 255–262.
[19] C.L. Souza, C.A.L. Chernicharo, S.F. Aquino, Quantification of dissolved methane in UASB reactors treating domestic wastewater under different operating conditions, Water Sci. Technol. 64 (11) (2011) 2259–2264.
[20] B.C. Crone, J.L. Garland, G.A. Sorial, L.M. Vane, Significance of dissolved methane in effluents of anaerobically treated low strength wastewater and potential for recovery as an energy product: A review, Water Res. 104 (2016) 520–531.
[21] J. Cookney, E. Cartmell, B. Jefferson, E.J. McAdam, Recovery of methane from anaerobic process effluent using poly-di-methyl-siloxane membrane contactors, Water Sci. Technol. 65 (4) (2012) 604–610.
[22] P. Sanchis-Perucho, Á. Robles, F. Durán, J. Ferrer, A. Seco, PDMS membranes for feasible recovery of dissolved methane from AnMBR effluents, J. Membr. Sci. 604 (2020) 118070.
[23] A. McLeod, B. Jefferson, E.J. McAdam, Toward gas-phase controlled mass transfer in micro-porous membrane contactors for recovery and concentration of dissolved methane in the gas phase, J. Membr. Sci. 510 (2016) 466–471.
[24] Q. Sohaib, C. Kalakech, C. Charmette, J. Cartier, G. Lesage, J.-P. Mericq, Hollow-fiber membrane contactor for biogas recovery from real anaerobic membrane bioreactor permeate, Membranes 12 (2) (2022) 112.
[25] S. Chen, W. Arnold, N. Wright, K. Zhu, O. Ajayi, P. Novak, Encapsulation technology for decentralized brewery wastewater treatment: A small pilot experiment, Bioresour. Technol. 347 (2022) 126435.
[26] X. Tan, G. Capar, K. Li, Analysis of dissolved oxygen removal in hollow fibre membrane modules: effect of water vapour, J. Membr. Sci. 251 (1–2) (2005) 111–119.
[27] M.-C. Yang, E.L. Cussler, Designing hollow-fiber contactors, AIChE J. 32 (11) (1986) 1910–1916.
[28] S. Wickramasinghe, M.J. Semmens, E. Cussler, Better hollow fiber contactors, J. Membr. Sci. 62 (3) (1991) 371–388.
[29] D.W. Johnson, M.J. Semmens, J.S. Gulliver, Unconfined membranes: Transfer performance and module design, J. Membr. Sci. 140 (1) (1998) 13–25.
[30] W. Rongwong, K. Goh, T.-H. Bae, Energy analysis and optimization of hollow fiber membrane contactors for recovery of dissolve methane from anaerobic membrane bioreactor effluent, J. Membr. Sci. 554 (2018) 184–194.
[31] R.O. Crowder, E.L. Cussler, Mass transfer resistances in hollow®ber pervaporation, J. Membr. Sci. (1998) 12.
[32] J. Patrick Montoya, Membrane Gas exchange: Using Hollow fiber membranes to Separate gases from Liquid and Gaseous streams, white Paper, MedArray, Inc., 2010, p. 7.
[33] S. Wickramasinghe, M.J. Semmens, E. Cussler, Mass transfer in various hollow fiber geometries, J. Membr. Sci. 69 (3) (1992) 235–250.
[34] C. Wang, E. Mercer, F. Kamranvand, L. Williams, A. Kolios, A. Parker, S. Tyrrel, E. Cartmell, E. McAdam, Tube-side mass transfer for hollow fibre membrane contactors operated in the low Graetz range, J. Membr. Sci. 523 (2017) 235–246.
[35] R.S. Subramanian, Notes on Transport Phenomena, Tech. rep., Clarkson University, 2020.
[36] J. Newman, Extension of the leve˘que solution, J. Heat Transfer 91 (1) (1969) 177–178.
[37] A. Popel, J. Gross, Mass transfer in the entrance region of a circular tube, Int. J. Heat Mass Transfer 21 (8) (1978) 1133–1141.
[38] T.L. Bergman, F.P. Incropera (Eds.), Fundamentals of Heat and Mass Transfer, Seventh ed, Wiley, Hoboken, NJ, 2011.
[39] M.L. Huber, R.A. Perkins, A. Laesecke, D.G. Friend, J.V. Sengers, M.J. Assael, I.N. Metaxa, E. Vogel, R. Mareš, K. Miyagawa, New international formulation for the viscosity of H2O, J. Phys. Chem. Ref. Data 38 (2) (2009) 101–125.
[40] C.R. Wilke, P. Chang, Correlation of diffusion coefficients in dilute solutions, AIChE J. 1 (2) (1955) 264–270.
[41] B.E. Poling, J.M. Prausnitz, J.P. O'Connell, Properties of Gases and Liquids, fifth ed., McGraw-Hill Education, New York, 2001.
[42] J.R. Rumble (Ed.), CRC Handbook of Chemistry and Physics, 103rd Edition (Internet Version 2022), CRC Press/Taylor & Francis, Boca Raton, FL, https://hbcp.chemnetbase.com/faces/documents/06_43/06_43_0001.xhtml.
[43] P.A. Witherspoon, D.N. Saraf, Diffusion of methane, ethane, propane, and n-butane in water from 25 to 43°, J. Phys. Chem. 69 (11) (1965) 3752–3755.
[44] H. Moradi, H. Azizpour, H. Bahmanyar, M. Mohammadi, M. Akbari, Prediction of methane diffusion coefficient in water using molecular dynamics simulation, Heliyon 6 (11) (2020) e05385.
[45] P. Han, D.M. Bartels, Temperature dependence of oxygen diffusion in H2O and D2O, J. Phys. Chem. 100 (13) (1996) 5597–5602, Publisher: American Chemical Society.
[46] K. Sharma, N.P. Adhikari, Temperature dependence of diffusion coefficient of nitrogen gas in water: A molecular dynamics study, Internat. J. Modern Phys. B 28 (14) (2014) 1450084.
[47] J. Huang, A simple accurate formula for calculating saturation vapor pressure of water and ice, J. Appl. Meteorol. Climatol. 57 (6) (2018) 1265–1272.
[48] P.T.H.M. Verhallen, L.J.P. Oomen, A.J.J.M.v.d. Elsen, J. Kruger, J.M.H. Fortuin, The diffusion coefficients of helium, hydrogen, oxygen and nitrogen in water determined from the permeability of a stagnant liquid layer in the quasi-s, Chem. Eng. Sci. 39 (11) (1984) 1535–1541.
[49] A. Ito, K. Yamagiwa, M. Tamura, M. Furusawa, Removal of dissolved oxygen using non-porous hollow-fiber membranes, J. Membr. Sci. (1998).
[50] M. Elimelech, W.A. Phillip, The future of seawater desalination: Energy, technology, and the environment, Science 333 (6043) (2011) 712–717.